

## Review

# Smart magnetic resonance imaging-based theranostics for cancer

Beatriz Brito<sup>1,2,3</sup>, Thomas W. Price<sup>1</sup>, Juan Gallo<sup>3</sup>, Manuel Bañobre-López<sup>3</sup>, Graeme J. Stasiuk<sup>1</sup>

1. Department of Imaging Chemistry and Biology, School of Biomedical Engineering and Imaging Sciences, King's College London, Strand, London, UK, SE1 7EH.
2. School of Life Sciences, Faculty of Health Sciences, University of Hull, Cottingham Road, Hull, UK, HU6 7RX.
3. Advanced Magnetic Theranostic Nanostructures Lab, International Iberian Nanotechnology Laboratory, Av. Mestre José Veiga, 4715-330 Braga.

 Corresponding authors: Manuel Bañobre-López (E-mail: manuel.banobre@inl.int) & Graeme J. Stasiuk (E-mail: graeme.stasiuk@kcl.ac.uk). Juan Gallo (E-mail: juan.gallo@inl.int)

© The author(s). This is an open access article distributed under the terms of the Creative Commons Attribution License (<https://creativecommons.org/licenses/by/4.0/>). See <http://ivyspring.com/terms> for full terms and conditions.

Received: 2020.12.10; Accepted: 2021.03.29; Published: 2021.08.07

## Abstract

Smart theranostics are dynamic platforms that integrate multiple functions, including at least imaging, therapy, and responsiveness, in a single agent. This review showcases a variety of responsive theranostic agents developed specifically for magnetic resonance imaging (MRI), due to the privileged position this non-invasive, non-ionising imaging modality continues to hold within the clinical imaging field. Different MRI smart theranostic designs have been devised in the search for more efficient cancer therapy, and improved diagnostic efficiency, through the increase of the local concentration of therapeutic effectors and MRI signal intensity in pathological tissues. This review explores novel small-molecule and nanosized MRI theranostic agents for cancer that exhibit responsiveness to endogenous (change in pH, redox environment, or enzymes) or exogenous (temperature, ultrasound, or light) stimuli. The challenges and obstacles in the design and *in vivo* application of responsive theranostics are also discussed to guide future research in this interdisciplinary field towards more controllable, efficient, and diagnostically relevant smart theranostics agents.

Key words: theranostics, responsive, smart, magnetic resonance imaging, cancer, contrast agents, therapy, nanoparticles, small molecules

## Introduction

Theranostics is an exciting new field of medicine that refers to the combination of diagnosis and therapy in a single molecule or entity [1]. Theranostic agents provide a way to image, characterize, and monitor molecular events while simultaneously delivering a specific therapy [1, 2]. These structures have the potential to improve the efficacy of treatment of several disorders, including different types of cancer [3, 4], neurodegenerative disorders [5-7], and cardiovascular diseases [8, 9], thus delivering better personalised medical care [3, 5, 8, 9]. Theranostic agents usually combine one or more therapeutic modalities, such as chemotherapy, radiotherapy (RT), photodynamic therapy (PDT), photothermal therapy (PTT), magnetic hyperthermia (MH), immunotherapy or chemodynamic therapy, with different imaging techniques, including magnetic resonance imaging

(MRI), positron emission tomography (PET), single photon emission computed tomography (SPECT), ultrasound (US), photoacoustic imaging (PA) or fluorescence imaging (FL) [1, 10, 11].

The combination of diagnosis/monitoring and therapy can offer synergistic advantages in comparison to standard imaging or treatment alone. Well-designed theranostic agents can facilitate the diagnosis and treatment of diseases at an early stage, provide valuable feedback of drug distribution to target sites and enable monitoring of the response to therapy [12, 13]. The efficiency of these theranostic agents is highly dependent on their therapeutic effect, thus several therapeutic modalities are often combined into a single agent [14-16]. The efficacy of theranostic agents' imaging capabilities greatly depends on their ability to accumulate at the target

site and induce a local enhanced contrast effect. Both the therapeutic and imaging indexes can be improved by designing targeted probes, usually through combination with targeting antibodies [17-19], peptides [20-22], or aptamers [23-25], and/or by designing “smart” responsive theranostic platforms [26-33]. The latter type of theranostic agents undergo structural or physicochemical alterations in response to a predefined stimulus (Figure 1) [26, 34].

Smart or responsive theranostics are platforms in which the therapeutic agent is ideally released/activated only after reaching the target tissue, in response to a certain stimulus. These stimuli can be caused by pathological conditions at the target sites compared to healthy tissues, such as changes in the pH, redox environment, overexpression of enzymes, or hypoxic conditions [26, 34]. Alternatively, smart theranostics can respond to locally induced external stimuli, such as irradiation with light [35-40] or

exposure to magnetic fields [41].

There have been several promising reports of smart theranostic agents for cancer using PET [47], FL [48, 49], and US [50] as the chosen imaging modality [51]. However, this review will focus on MRI-based responsive theranostics that are specific for cancer, as MRI is one of the preferred clinical imaging techniques in the diagnosis of this pathology [52-55]. This review will also feature relevant dual modal imaging theranostic agents featuring MRI as one of the imaging technologies. We will first review examples of different strategies that have been exploited to design targeted and/or smart contrast agents. Then, we will show how some of those strategies, as well as other novel approaches, have been employed to design a wide range of smart MRI theranostics, which will be divided according to the stimuli that induces drug release and/or magnetic resonance (MR) signal switch. Additionally, we will comment on the

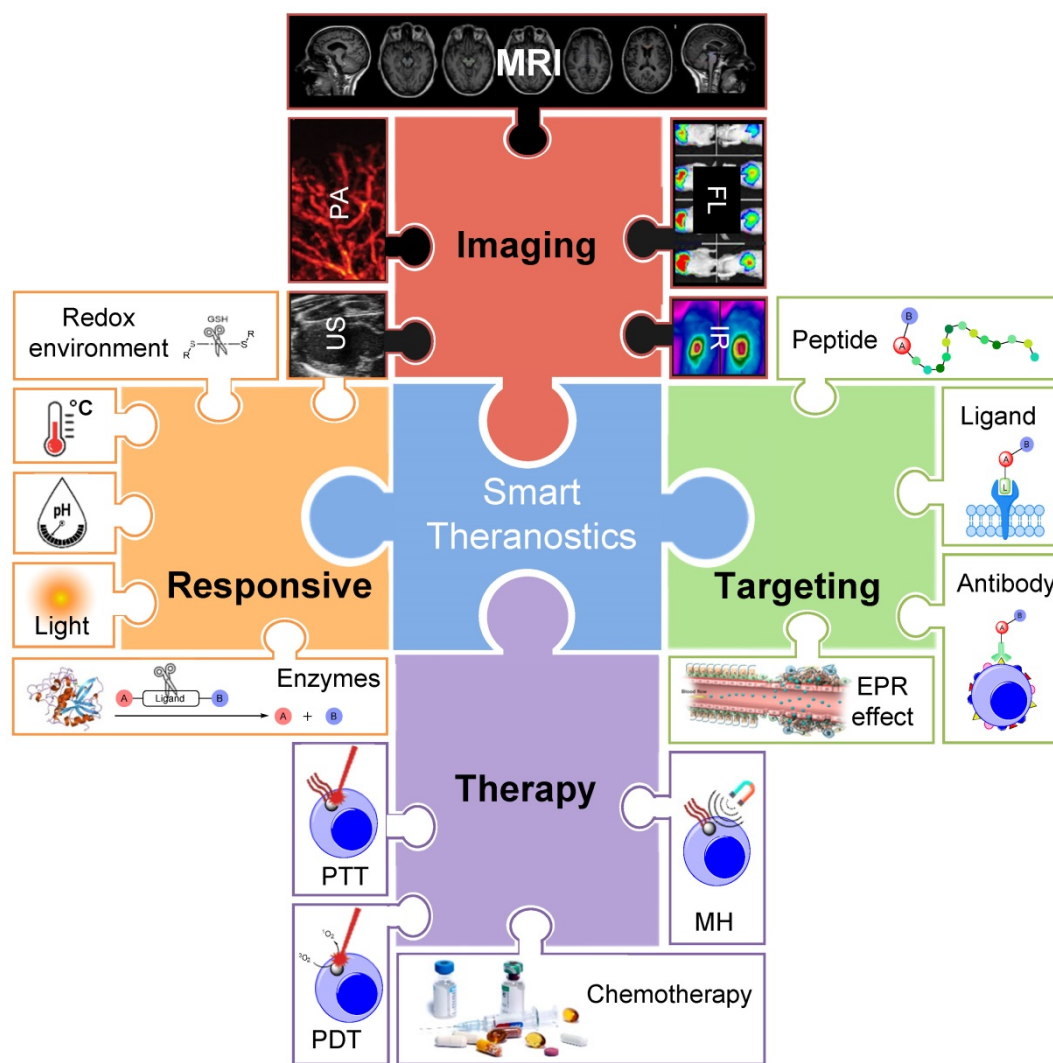


**Figure 1.** Illustration representing some of the key components of a smart theranostic platform. Smart theranostic systems need to combine contrast agents for distinct imaging modalities, a targeting strategy, therapy effectors and responsive moieties. Adapted with permission from [42-46], copyright 2020 Moran and Thomson, 2018 Stylogiannis et al, 2020 Picillo et al, 2013 Cheng et al, 2016 Tang et al.

obstacles that have so far hindered the clinical implementation of these agents, which include specific targeting limitations, the low sensitivity of the imaging component and reduced biocompatibility. Finally, novel strategies that could be used to overcome these drawbacks will be presented.

## Magnetic Resonance Imaging

MRI is a non-invasive, non-ionising, tomographic imaging modality that is particularly useful to detect and characterize soft tissue pathologies [56, 57]. MRI provides three-dimensional (3D) images with high spatial resolution, high penetration and high contrast [56]. This makes MRI one of the first choices for clinical diagnosis and monitoring of a wide range of disorders, including cancer, heart disease and neurological or musculoskeletal disorders, among others [52, 58, 59].

The term “MRI” usually refers to proton ( $^1\text{H}$ ) MRI, which makes use of nuclear properties of water protons present in the body, such as the nuclear spin, to generate images [55]. There are other MRI techniques that are sensitive to heteroatoms like fluorine ( $^{19}\text{F}$ ), carbon ( $^{13}\text{C}$ ) or sodium ( $^{23}\text{Na}$ ) [60].  $^{19}\text{F}$ -MRI in particular is being explored as a promising imaging tool [61].

### Basic principles of MR

The basic principles of heteroatom MRI are similar to those of  $^1\text{H}$  MRI, which are detailed in several reviews and book chapters [55, 56, 62-64]. Briefly, after exposure to an external magnetic field ( $B_0$ ), the magnetic moments of the nuclear spins of water protons align along the longitudinal plane. Then, a radiofrequency (RF) pulse is used to energise the system and to “flip” the magnetic moment of proton nuclei towards the transversal plane. Once the RF pulse is turned off, the transverse magnetisation decays over time through a process known as relaxation, which generates the signals that can be reconstructed into 3D images [56, 63]. The relaxation process follows two distinct, independent, and simultaneous pathways:  $T_1$  and  $T_2$  relaxation [52, 56]. Different tissues in the body have distinct  $T_1$  and  $T_2$  relaxation times and this difference is exploited to create contrast in MR images [52]. However, given the high abundance of water molecules in the body, the signal-to-background ratio of MRI is very low. This contributes to the intrinsic low sensitivity of MRI [52].

### MRI contrast agents

Contrast agents (CAs) have been widely used to enhance contrast between tissues and help overcome the sensitivity issue, thus facilitating the diagnosis of different pathologies [65, 66]. MRI CAs usually have

electronic configurations with unpaired electrons that change local nuclei relaxation time and generate extra contrast in MRI. These MRI CAs can be divided into two categories, depending on their effect on the relaxation of the signal:  $T_1$  agents or  $T_2$  agents [56, 67].

$T_1$  agents shorten predominantly the  $T_1$  relaxation time by withdrawing excess energy from the spin-lattice. This fast recovery of longitudinal magnetisation leads to the production of a strong MR signal and translates into brighter images.  $T_1$  agents are usually paramagnetic complexes of the lanthanide ion gadolinium ( $\text{Gd}^{3+}$ ), or of the transition metal ion manganese ( $\text{Mn}^{2+}$ ) [68-84]. There have also been reports of nanoparticles acting as  $T_1$  enhancers, including  $\text{Gd}^{3+}$ -based nanoparticles, extremely small iron oxide nanoparticles (ESIONs) and Mn-based nanoparticles [85-90].

Other CAs exert a higher effect on  $T_2$  than  $T_1$  relaxation, therefore they are referred to as  $T_2$  agents [52]. These agents shorten the  $T_2$  relaxation time, leading to a faster dephasing, which is caused by an increase in spin-spin interactions between the water protons and the CA. The shortening of  $T_2$  leads to the production of a weaker MR signal and, consequently, to the procurement of darker images. These agents are typically superparamagnetic iron oxide nanoparticles (SPION) [91-93].

The efficacy of  $T_1$  and  $T_2$  contrast agents can be determined by their relaxivity ( $r_1$  and  $r_2$ , respectively), which describes the extent to which a CA can affect the relaxation rate of water and is measured in per millimolar per second ( $\text{mM}^{-1} \text{s}^{-1}$ ) [52, 59].

Even though MRI CAs significantly increase the contrast between tissues and are a valuable diagnostic tool, the inherent low sensitivity of MRI is still a problem [52]. In order to overcome this limitation, there has been an increasing interest in the design of CAs with high relaxivity and/or that specifically accumulate in the tissue of interest [52, 83, 84]. As an alternative, the design of switchable MRI CAs has also been explored to increase the signal-to-background ratio at the target site [52, 77, 86, 94-98].

## Smart Theranostics for Cancer

Smart theranostics are usually made of at least two components, the therapeutic and the imaging agent moieties, where at least one of them is responsive to environmental conditions or to external stimuli. Smart theranostics can be classified based on the nature of the stimulus (e.g. pH responsive smart theranostics), which is how this review approaches them. However, it is also important to differentiate smart theranostics based on the component that is changed upon exposure to said stimulus (Figure 2).

Both the imaging and therapy components can

be altered by a trigger, sometimes simultaneously. Theranostics with responsive therapeutic effect can be divided into two categories: a) smart theranostics with environmentally activated therapy, in which the drug release and/or therapeutic efficacy is triggered by an endogenous signal, e.g. altered enzymatic expression profiles, high glutathione (GSH) concentrations, acidic conditions, or aberrant hypoxia in tumours [26, 34, 99-104]; or b) smart theranostics with remotely activated therapy, in which the therapeutic response is triggered by an external signal, e.g. light for PDT agents.

Smart theranostic platforms can also include switchable contrast enhancing components in which the signal enhancement of the imaging agent moiety responds to environmental triggers by switching from off/ON, ON/off or on/ON as the drug is released. In the first type of smart CAs, the relaxation enhancement changes from an “off” state, where contrast enhancement is negligible, to an “ON” state with a significantly higher contrast enhancement. CAs can also undergo stimuli-dependent changes that significantly decrease their relaxivity and contrast enhancement; they are described as ON/off smart CAs. The on/ON contrast switch is common for small-molecule based CAs and describes the change from a state with a relevant, albeit low, relaxation enhancement (“on” state) to one with significantly higher relaxation enhancement (“ON” state). These platforms are classified in this review as smart theranostics with environmentally switchable contrast agents. This classification of theranostics allows for a more efficient monitoring of drug release and response to treatment, better understanding of drug distribution and better chance to personalise treatment, which, in turn, can positively impact patient prognosis.

A smart theranostic agent can be made of a combination of these types. For example, Liu *et al.* designed nanowreaths for PTT and MR that contained imaging agents that were released in response to GSH to impact image contrast, as will be explained later [105]. As such, this is an example of a smart theranostic platform with remotely activated therapy and environmentally switchable CAs.

In terms of the characteristics that constitute an ideal smart theranostic agent for cancer, these platforms should aspire to satisfy the requirements for both optimal contrast agents for MRI and excellent therapeutic effectors for the targeted disease, while also being responsive to a specific trigger [106]. However, this can be exceedingly difficult to achieve and, as such, the optimised smart theranostic design will most likely result from a compromise of some properties in favour of others. Still, an ideal smart MRI theranostic for cancer should, in broad terms:

- Present good physicochemical stability, biocompatibility and biodegradability;
- Induce strong contrast enhancement;
- Have increased and specific tumour uptake and accumulation;
- Have higher toxicity towards cancer cells versus normal cells;
- Undergo an emphatic change in response to an endogenous or controllable stimulus;
- Have sufficiently long blood circulation time to accumulate at target sites but not so long as to trigger safety concerns.

In this next section, we will explore different theranostic platforms and discuss their advantages and disadvantages.

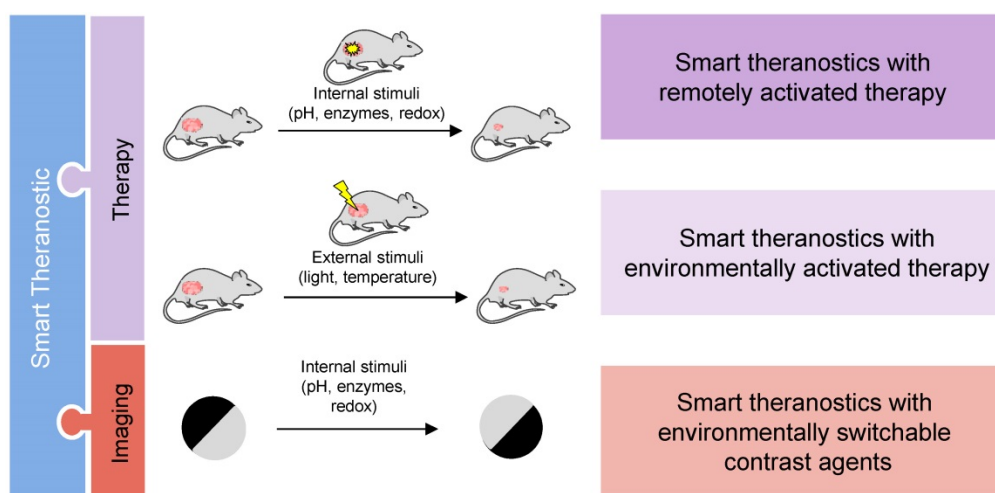


**Figure 2.** Schematic of the different classifications given to smart theranostic agents based on the effect of the stimulus on their imaging and therapeutic moieties.

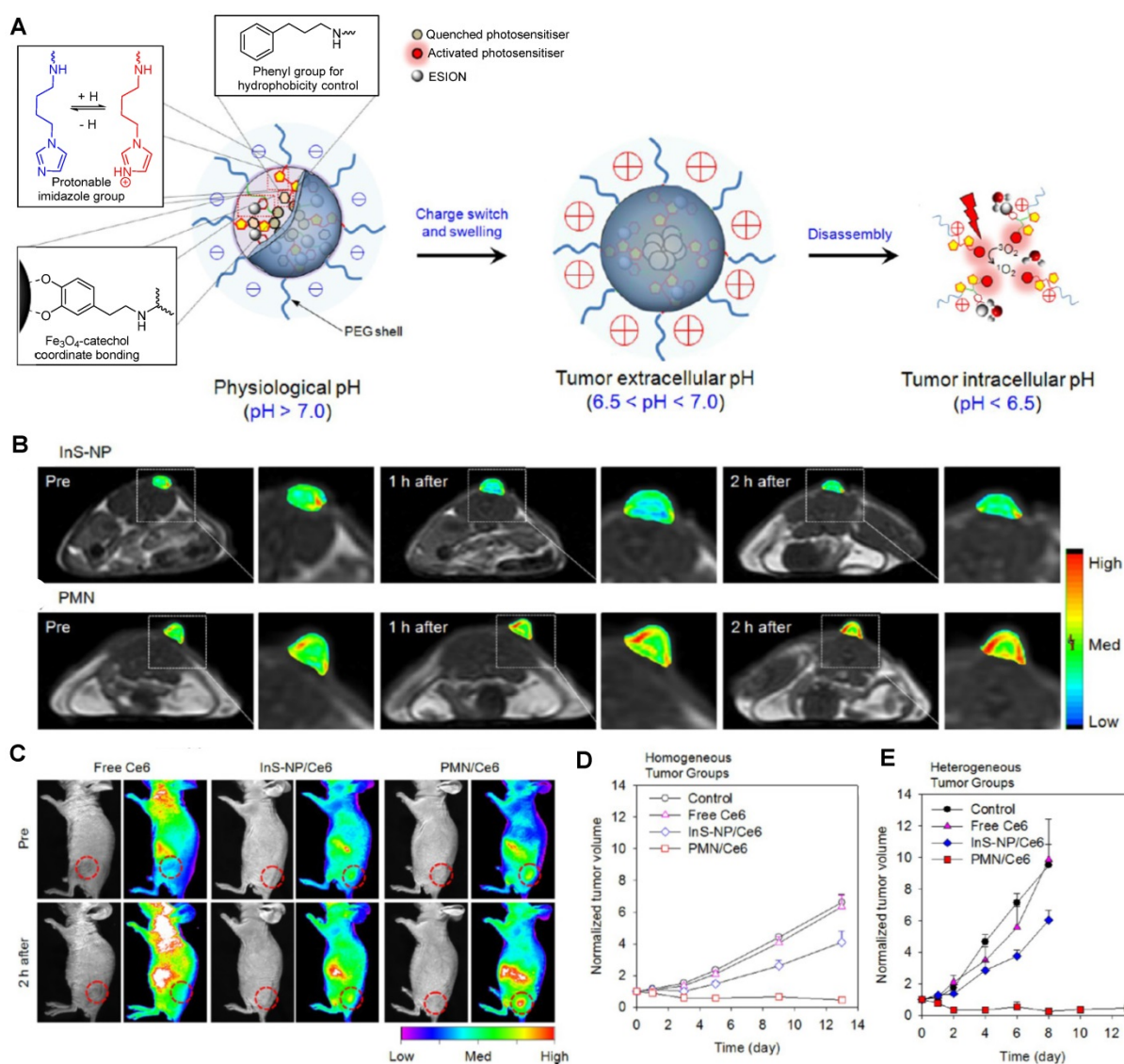


**Figure 3.** A. Schematic illustration of pH-dependent structural transformation of PMNs. The theranostics are latent in the circulation and then the surface charge switches from negative to positive in response to the low pH at the tumour microenvironment, which facilitates tissue permeation and triggers cell internalisation, after which the even more decreased pH induces further disassembly to enhance the MRI contrast and photoactivity of the PMNs. B. *In vivo*  $T_1$ -weighted MR images and colour-mapped images of tumour sites before, 1 h after, or 2 h after intravenous injection of PMNs or InS-NPs (2 mg Fe kg<sup>-1</sup>) into nude mice bearing 3–5 mm HCT116 tumours at 1.5 T. C. *In vivo* NIR imaging of nude mice bearing HCT116 tumours after intravenous injection of PMNs, InS-NPs or free Ce6 (equivalent to 0.2 mg kg<sup>-1</sup> Ce6). D. Homogeneous HCT116 and E. heterogeneous CT26 tumour volumes after treatment with saline (control), free Ce6, InS-NPs and the nanogrenades (PMN/Ce6), followed by irradiation of the tumour regions with a 670 nm laser (250 mW cm<sup>-2</sup>, 20 min) 12 h post injection and 5 days after that. Adapted with permission from [113], copyright 2014 American Chemical Society.

## pH responsive smart theranostics

The pH of the tumour microenvironment is more acidic than that of normal tissues ( $pH_{\text{tumour}} = 6.4\text{--}7.0$ ,  $pH_{\text{healthy}} = 7.2\text{--}7.5$ ) [107, 108]. This can be exploited to design pH responsive theranostic systems that preferentially release their cargos at lower pH. These platforms usually present at least one component that is ionizable at low pH, and thus induces a physical transformation of nano-based agents that leads to drug release and/or induces a change in the relaxivity of the MR moiety. Other pH-responsive strategies make use of pH-sensitive chemical bonds [109, 110] or acid-degradable nanocomposites to induce drug release and/or relaxation changes [102, 111, 112].

Several pH-responsive theranostic agents have been proposed [32, 113–118].

For example, Ling *et al.* synthesised what they called pH-sensitive magnetic nanogrenades (PMNs) that showed pH-sensitive MRI and fluorescence contrast enhancement and could be used for PDT [113]. These nanosystems were synthesised by self-assembly of extremely small iron oxide nanoparticles (ESIONs, 3 nm diameter), porphyrin-like photosensitizers for PDT (chlorin e6, Ce6) and contained pH responsive ionizable moieties, polyelectrolytes, on the surface (Figure 3A). These PMNs work in a two-stage pH dependent activation. At physiological pH, the stable nanoparticles are negatively charged. However, when the nanoparticles extravasate to the acidic

tumour microenvironment (pH = 6.4-7.0), the polarity of the complex is reversed, due to the ionization of imidazole groups on their surface, which potentiates the increase of electrostatic interactions with anionic cells and subsequent cell internalisation of the complexes into endosomes. Inside endosomes, the pH is lower than 6.5, which triggers complete dissociation of the theranostic platforms.

This is accompanied by an increase in the  $r_1$  of PMNs, due to higher protonation of ligands as the pH decreases and consequent increase of water molecules coordinated to  $\text{Fe}^{3+}$  ions on the surface of ESIONs. The  $r_2/r_1$  ratio similarly decreases during the pH-responsive disassembly process, which contributes to the recovery of  $T_1$  MR signal at pH = 5.5 and thus allows for pH sensitive  $T_1$  contrast enhancement. The accumulation of PMNs inside tumour cells can be observed in the  $T_1$  weighted and NIR images in Figure 3B and C, where a contrast enhancement in both imaging modalities can be seen. This contrast is even perceptible in ultrasmall tumours (3-5 mm) and it is much more notable for the PMNs than for pH-insensitive nanoparticle assemblies (InS-NP). The therapeutic efficiency of these theranostic agents for PDT was also evaluated. Irradiation with a 670 nm laser 12 h after injection with PMN/Ce6 nanosystems led to the destruction of tumour tissue, microvasculature, and fibroblasts in both homogeneous and heterogeneous tumours, unlike irradiation after treatment with pH-insensitive nanoparticle assemblies. This is mainly due to the activation of the self-quenched photosensitisers of the PMN/Ce6 platforms at the low pH of tumour cells or microenvironment. This is an example of responsive nanoplatfroms with environmentally (pH) switchable imaging agents and remotely (light) activated therapy, in which pH targeting plays a vital role in improving their imaging properties and therapeutic efficacy.

ESIONs were also used in the design of pH-responsive MRI theranostics that targeted integrin-expressing cancer cells [119]. Shen *et al* first synthesised ESIONs by co-precipitation with poly(acrylic acid) (PAA) and studied the effect of the size of the nanoparticles on their relaxivity. The nanoparticles with the best imaging potential (3.6 nm) were then conjugated with a RGD peptide. Poly(ethylene glycol)methyl ether (mPEG) was grafted to the nanoparticles through an acid-labile  $\beta$ -thiopropionate linker, which was followed by conjugation of DOX. This smart design ensures that the integrin ligand is hidden in the mPEG "stealth" layer until the nanoparticles reach the acidic tumour microenvironment, at which point the linker holding the mPEG to the NPs is broken and the exposed RGD peptide binds to  $\alpha_v\beta_3$ -expressing cancer cells.

Treatment of U87MG tumour-bearing mice with these DOX@ES-MION3@RGD<sub>2</sub>@mPEG3 constructs showed that the nanoparticles had high MRI imaging efficiency, likely due to high tumour accumulation, and high therapeutic efficacy, since tumour growth was effectively suppressed in all treated mice. This constitutes an example of a biocompatible theranostic with environmentally responsive and targeted drug delivery in which the MR contrast enhancement in tumours is improved by the pH-dependent accumulation on these sites.

Although these iron-based nanoparticles should be more biocompatible than some of the available alternatives (e.g. Gd-based systems), they could still cause toxic effects *in vivo*. The toxicity of these type of nanoparticles is usually dependent on specific characteristics of the nanoparticles, including chemical composition, size and surface to volume ratio, immunogenicity, and pharmacokinetics [120]. As such, these factors should be carefully studied in smart theranostic design.

He *et al.* also designed theranostic agents with environmentally (pH) activated therapy by loading gadolinium oxide ( $\text{Gd}_2\text{O}_3$ ) nanoparticles as MRI agents and doxorubicin (DOX) as a chemotherapy drug inside mesoporous silica nanoparticles (MSNs) modified with polyelectrolytes and folic acid on the surface [115]. These nanoplatfroms enter cells specifically by folic acid receptor mediated endocytosis and accumulate inside endosomes. The acidic pH of endosomes triggers the disintegration of the polyelectrolytes on the surface of the nanoparticles and leads to the release of DOX, which was confirmed by time-resolved fluorescence microscopy. The MRI contrast is also increased for these targeted systems, due to the accumulation of  $\text{Gd}_2\text{O}_3$  nanoparticles ( $r_1 = 9.14 \text{ mM}^{-1} \text{ s}^{-1}$  at 3.0 T) inside folic acid receptor expressing cells. In these types of  $\text{Gd}^{3+}$ -based nanosystems, as well as in  $\text{Gd}^{3+}$  complexes, the stability, biosafety and biocompatibility should be ensured, as Gd-based CAs have been linked to nephrogenic systemic fibrosis (NSF) and free  $\text{Gd}^{3+}$  ions are known to be toxic [121, 122].

Recently, Wu *et al.* fabricated a chelate-free, pH responsive nanoscale coordination polymer with  $\text{Mn}^{2+}$  ions coordinated to chemotherapy drug methotrexate (MTX) and coated with PEG (MTX-Mn@PEG, Figure 4A) [117]. Pharmacokinetic assays in mice showed that these nanoparticles had enhanced circulation half-life, as they lasted up to  $4 \pm 2$  h in blood (in comparison,  $\text{MnCl}_2$  lasted only  $0.71 \pm 0.15$  h). This increase in blood circulation was attributed to the stabilising effect of the PEG coating and means that the particles have more time to accumulate in the tumour site through the enhanced permeability and retention (EPR) effect,

which leads to a contrast enhancement in MRI that can last up to 24 h post injection in mice (Figure 4B). The pH dependent drug release mechanism was also investigated. The authors attributed the faster drug release at low pH (48.9% release after 4 h at pH = 5.5 versus 33.2% release after 12 h at pH = 7.4) to the loss of coordination of  $Mn^{2+}$  to the chemotherapy drug, following protonation of the carboxylic groups and nitrogen heterocycle of MTX at low pH. This pH dependent mechanism and the accumulation of the MTX-Mn@PEG nanoparticles at the tumour sites contributed to a more efficient tumour regression than treatment with MTX alone, as seen on Figure 4C, D and E.

This is a rather straightforward method to synthesise theranostic nanosystems for cancer therapy that can be adapted to other drugs, metals, or even other imaging modalities. However, the pH that induces drug release (pH = 5.5) is relatively low when compared to the pH of most tumour microenvironments (pH = 6.4-7.0), which limits the responsiveness of the system, as the drug is probably only released following cellular uptake. It is also important to consider the thermodynamic and kinetic stability of the metal-drug complexes, as other paramagnetic metals, such as  $Gd^{3+}$ , can present serious toxicity problems upon complex dissociation

[123-127]. Indeed, even free  $Mn^{2+}$  can impart neurotoxicity in mice and has a median lethal dose ( $LD_{50}$ ) of  $0.3 \text{ mmol kg}^{-1}$  in these animals when injected intravenously [70]. Even though it is unlikely that this  $LD_{50}$  will be reached after administration of  $200 \mu\text{L}$  of  $MnCl_2$  ( $0.23 \text{ mg mL}^{-1}$ ) or of the nanotheranostic ( $1 \text{ mg mL}^{-1}$ ), the dosage of MTX-Mn@PEG nanoparticles still needs to be carefully considered.

pH-responsive theranostics can also be fashioned for PTT and/or PDT. For example, Wang *et al.* designed a theranostic nanosystem that could be used for MRI/near infrared imaging (NIR)-guided PTT/PDT of triple negative breast cancer [116]. This work aimed to develop theranostic platforms for the diagnosis of tumour location and precise phototherapy navigation, as well as for the determination of the therapeutic window of time and prognosis. Their pH-responsive theranostic nanosystem was composed of a hydrophobic core made of SPIONs and IR780 dye, surrounded by a hydrophilic crown (SPA, Figure 5A) of stearic acid, polyethylenimine (PEI) and hexahydrophthalic anhydride (HHPA). The responsiveness of the theranostic is introduced by the SPA matrix, which dissociates in the presence of a faintly acidic environment (pH = 6.5). At this pH, the amido bond between PEI and HHPA is broken, which exposes the positively charged amino groups to the

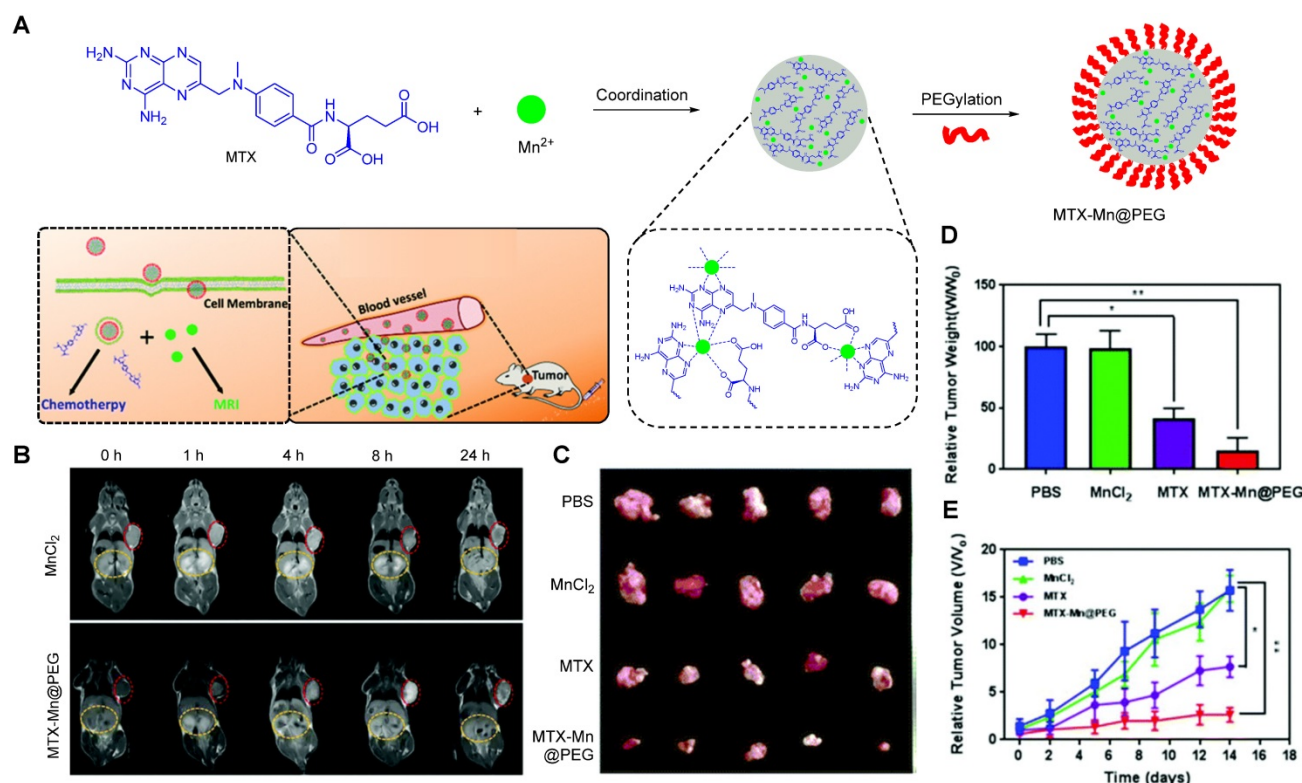


**Figure 4.** **A** Schematic illustration of the composition of MTX-Mn@PEG nanocapsules and their use as a theranostic nanoplatform for MRI guided chemotherapy. **B** *In vivo*  $T_1$  MR images of  $MnCl_2$  and MTX-Mn@PEG at different times post injection; red circles indicate the tumour and yellow circles indicate the kidneys of the mice, at 0.5 T. **C** Photographs of tumours excised from mice after 14 days of treatment. **D** Relative tumour weight of each group compared to the PBS group. **E** Relative tumour volumes of mice during the treatment. Adapted with permission from [117], copyright 2013, Royal Society of Chemistry.

outside of the nanosystem. This increases the electrostatic interactions between the nanosystems and the cancer cells, which leads to a higher cellular uptake in 4T1 (triple negative breast cancer) tumours in mice, as can be seen by the NIR and colour-mapped MR images (Figure 5B and C). The MRI contrast effect is more pronounced at the tumour site after treatment with SPA-SPIO-IR780 nanoparticles than with pH unresponsive probe (SP-SPIO-IR780), which can be explained by the pH-induced accumulation in tumours and by the large  $r_2$  of these particles ( $254.09 \text{ mM}^{-1} \text{ s}^{-1}$  at 1.5 T versus  $98.4 \text{ mM}^{-1} \text{ s}^{-1}$  for commercial CA Resovist®).

In terms of therapeutic efficiency, the treatment of mice with SPA-SPIO-IR780 nanoparticles followed by exposure to a NIR (780 nm) laser for 5 minutes led to a significant reduction of the tumour volume when compared to light excitation after treatment with PBS (tumour volume after 20 days was  $255.2 \text{ mm}^3$  and  $2563.7 \text{ mm}^3$ , respectively). As such, this is a promising theranostic nanoplatform with remotely activated therapy that uses the responsiveness of the matrix polymer to enhance tumour uptake and the therapeutic outcome of PTT/PDT.

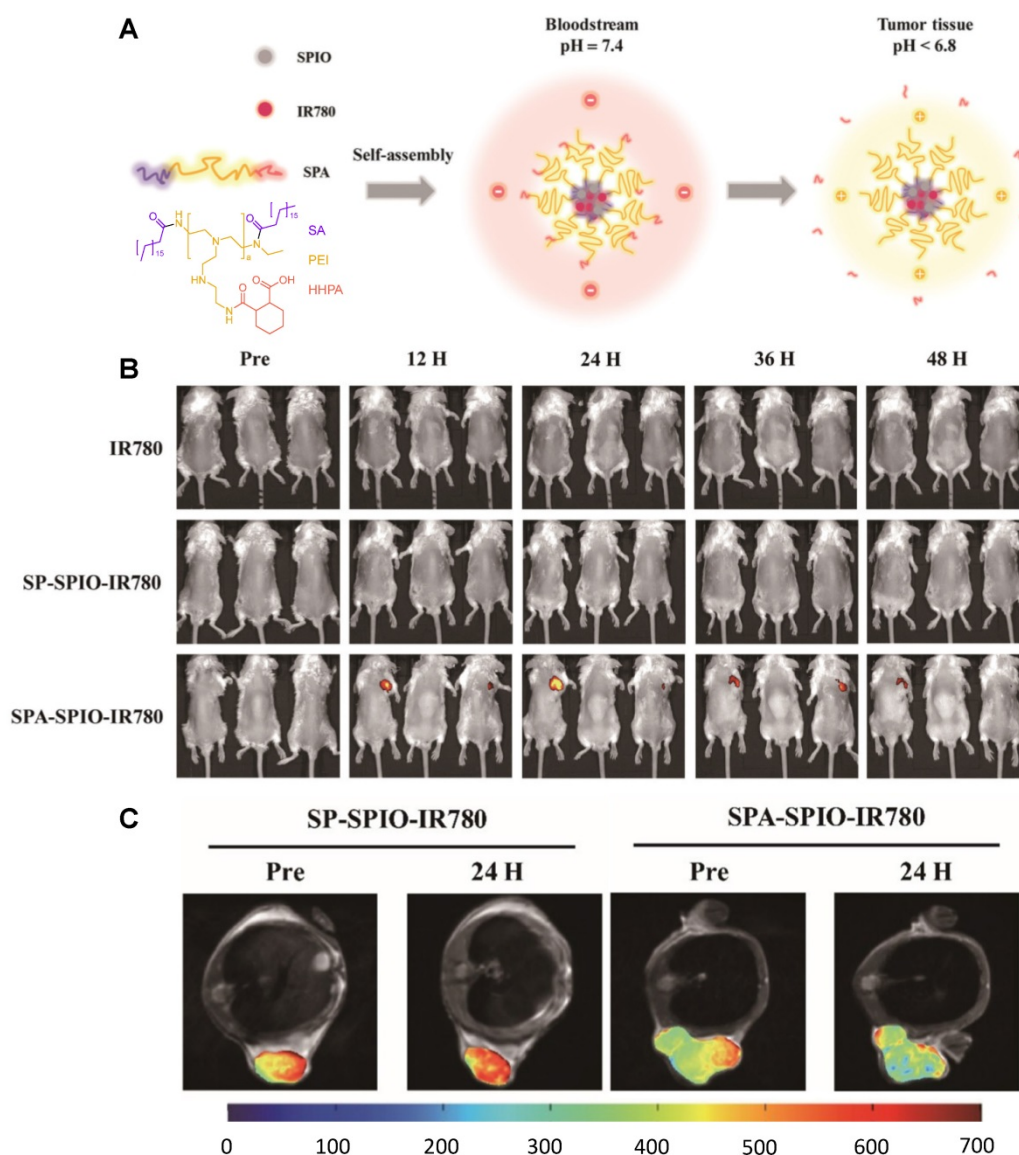


**Figure 5.** **A** Schematic illustration of the mechanism of the pH-sensitive nanotheranostic system. (SPIO: superparamagnetic iron oxide nanocrystals, SA: stearic acid, PEI: polyethylenimine, HHPA: hexahydrophthalic anhydride, SPA: hexahydrophthalic anhydride modified stearic acid-grafted polyethylenimine. **B** Time-lapse NIR images of mice treated with IR780, SP-SPIO-IR780 or SPA-SPIO-IR780 nanosystems, respectively. **C** MRI (colour mapping) of the tumour site before and 24 hours post-injection of SP-SPIO-IR780 and SPA-SPIO-IR780, 3.0 T. Adapted with permission from [116], copyright 2013 Royal Society of Chemistry.

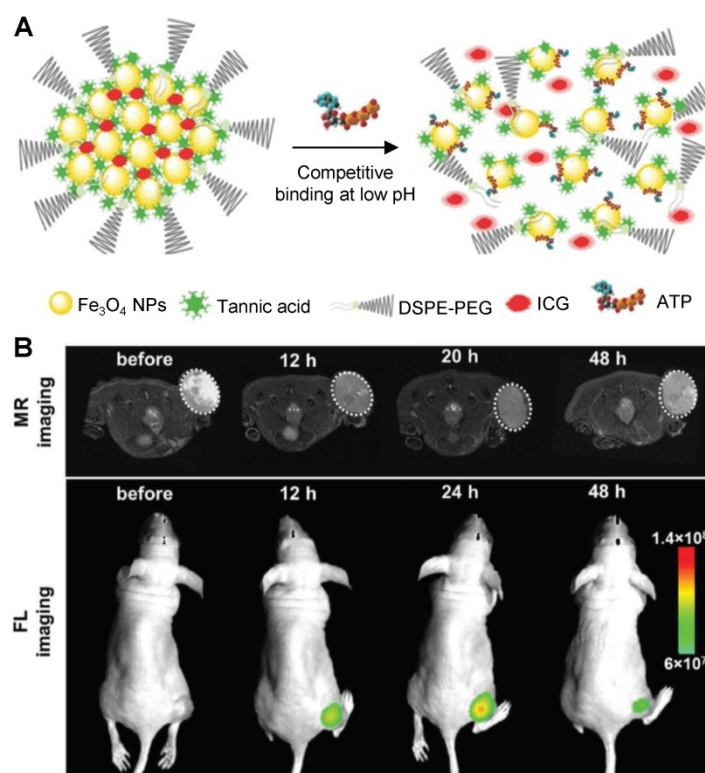


**Figure 6.** **A** Schematic illustration of the disassembly process suggested by Song *et al.* [32]. **B**  $T_2$ -weighted MR images and fluorescence images of HepG2 tumour-bearing mice after intravenous injection of the  $\text{Fe}_3\text{O}_4$ @TA-PEG/ICG assemblies at 7.0 T. Adapted with permission from [32], copyright 2017, John Wiley and Sons.

### Dual pH and other stimuli-responsive smart theranostics

Smart theranostics for PTT using MRI and FL have also been designed to exhibit ATP-responsive pH-facilitated disassembly (Figure 6A) [32]. These nanoconstructs were based on iron oxide nanoparticles, tannic acid (TA) and indocyanine green (ICG) surrounded by polyethylene glycol-modified distearyl phosphatidyl ethanolamine (DSPE-PEG). These particles responded to ATP (upregulated in tumours) because it binds competitively to the surface of SPIONs by displacing the TA holding the assemblies together. They also responded to low pH, due to protonation of hydroxyl groups on TA and subsequent weakening of the coordination bonds between polyphenols in TA structure and metals from the iron-based particles, which loosens the assemblies. This mechanism brought an associated dramatic change in transverse relaxivity upon disassembly (from  $r_2 = 251.2 \text{ mM}^{-1} \text{ s}^{-1}$  at  $\text{pH} = 7.4$  to  $r_2 = 13.68 \text{ mM}^{-1} \text{ s}^{-1}$  in the presence of 10 mM of ATP and at  $\text{pH} = 5.5$ ), which was accompanied by a large “turn-on” of fluorescence signals (Figure 6B). The switch in the FL signals can be attributed to the loss of the quenching effect induced by the magnetite nanoparticles on ICG following disassembly of the constructs upon treatment with ATP. Furthermore, injection of the nanoparticles in HepG2 tumour bearing mice initially

led to a slight darkening effect in MR images of the tumour region, due to the accumulation of a small number of intact assemblies at the target site (Figure 6). However, as the nanoplateforms encounter ATP in the cancerous tissues, the dark contrast effect decreased, due to ATP-induced disassembly. This also explains the increase in the fluorescence signals. Although the decrease in the brightness of the MRI contrast might be insufficient for a reliable diagnosis (as the clearance of the particles from the tumour will have the same effect on MR images), this mechanism allows for an easy detection of target sites using FL, since the signal intensity increases upon exposure to the stimuli. In terms of therapy, irradiation of treated mice with an NIR laser ( $808 \text{ nm}$ ,  $1 \text{ W cm}^{-2}$ ) led to a temperature increase of almost  $20 \text{ }^\circ\text{C}$  in the tumours and translated into remarkable ablation of tumour size with no tumour recurrence post treatment for 16 days. This study is then an example of multi-stimuli responsive multimodal theranostics offering remotely activated therapy and environmentally switchable MRI and FL.

Ren *et al.* designed another multi-stimuli theranostic probe that they described as an “all-in-one” agent, since it combined seven distinct functionalities: MRI, Computed Tomography (CT) and PA imaging, and PTT, PDT, chemotherapy and RT [118]. Their PEGylated doped metal chalcogenide nanoflowers were loaded with DOX (Bi- $\text{MS}_x$ -

PEG/DOX NFs) and contained either bismuth (Bi), manganese (Mn) or molybdenum (Mo). Depending on the dopant, these nanoflowers could be used for MR/CT/PA-guided PTT/PDT/RT/chemotherapy and responded to pH, NIR light and X-rays. The nanoflowers were used for chemotherapy since they had a high DOX loading (DOX loading weight percentage of around 90% at 1:1 feeding mass ratio of DOX to NF) and released 80% of loaded DOX within 8 h in response to low pH (pH = 5.5) and exposure to a NIR laser. The petal structure of the nanoflowers enhanced their photoabsorption properties, translating into a high photothermal efficiency (54.7%) and thus making them useful as PTT effectors. Bi-MS<sub>x</sub>-PEG nanoflowers could also be used for PDT, as they contained MoS<sub>2</sub> and Bi<sub>2</sub>S<sub>3</sub> composites able to generate <sup>1</sup>O<sub>2</sub> upon exposure to an 808 nm laser. Nanoflowers with abundant Bi could also induce DNA damage to cells upon exposure to X-rays, since Bi has strong X-ray attenuation capacity and could thus be used for RT. In terms of imaging, these nanoflowers could work as T<sub>1</sub> agents for MRI (due to the presence of Mn<sup>2+</sup> ions), as contrast enhancers for CT imaging (since Bi and Bi<sub>2</sub>S<sub>3</sub> efficiently absorb ionising radiation), or as photoacoustic imaging agents (as MoS<sub>2</sub> provides high and wide NIR optical absorbance). This novel “all-in-one” nanoplatform features both environmentally and remotely activated therapy and shows promising results in tumour ablation in mice. However, its efficacy as a multimodal imaging agent will greatly depend on the lifetime of the nanoconstructs in the bloodstream and inside cancer cells. Additionally, its pH activated therapy will depend on the NFs’ ability to enter tumour cells, as the pH that they respond to (pH = 5.5) is lower than that of the tumour microenvironment.

pH-responsive MRI theranostic agents for chemodynamic therapy (CDT) have also been designed. CDT is a novel ROS-based cancer treatment that utilises iron-mediated Fenton chemistry to destroy tumour cells by converting endogenous H<sub>2</sub>O<sub>2</sub> into toxic hydroxyl radicals (•OH). Xiao *et al.* synthesised nanoselenium-coated manganese carbonate-deposited iron oxide nanoparticles (MCDION-Se) that responded to the low pH of tumour microenvironments [128]. At pH = 5.5, the nanoplatforms released Mn<sup>2+</sup> ions, which increased the r<sub>1</sub> from 2.7 mM<sup>-1</sup> s<sup>-1</sup> (pH = 7.4) to 7.1 mM<sup>-1</sup> s<sup>-1</sup> (at 9.4 T). Following injection and pH-mediated release of Mn<sup>2+</sup>, the loaded nano-Se particles promoted the activation of superoxide dismutase (SOD) and consequent formation of H<sub>2</sub>O<sub>2</sub> and OH radicals for CDT. Treatment of cervical tumour-bearing mice with MCDION-Se theranostics slowed down tumour progression but did not inhibit tumour growth, which

suggests that a synergistic therapy approach could be considered in future works involving CDT to improve prognosis.

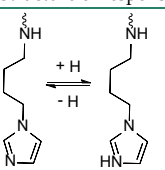
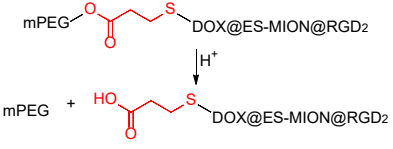
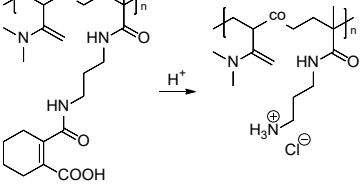
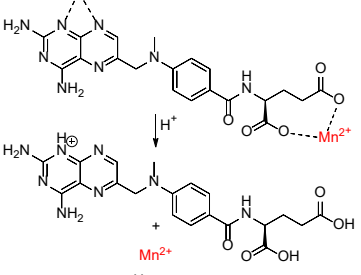
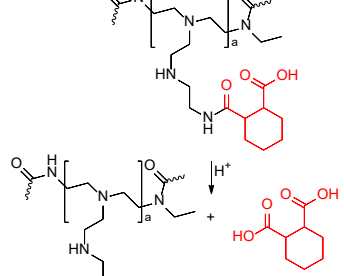
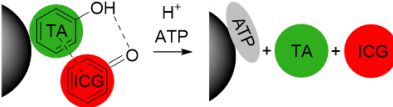
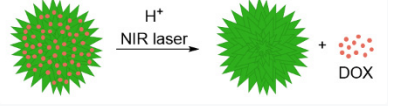
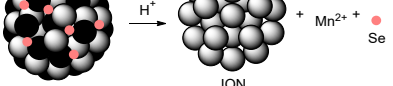
Small-molecule theranostics have found promising applications in cancer therapy [129-131]; their structure is more straightforward than that of most nanoparticles and their synthesis is more reproducible. In 2016, Lee *et al.* reported a pH-responsive small-molecule MRI theranostic for cancer therapy [132]. This system was equipped with a DOX prodrug conjugated to a Gd<sup>3+</sup>-texaphyrin complex *via* a pH-cleavable hydrazone linker. When intact, this complex was only weakly fluorescent, since DOX was quenched by the Gd<sup>3+</sup>-texaphyrin moiety. However, the fluorescence signal at 593 nm was switched from OFF to ON at low pH (pH = 5.0), due to the cleavage of the linker and separation of quencher and emitter. *In vitro* confocal microscope experiments with cancerous (A549 and CT26) and healthy (NIH3T3) cell lines showed that the Gd-texaphyrin-DOX complex was preferentially taken up by cancerous cells and was then hydrolysed inside lysosomes. Further studies indicated that this complex could also be used as a T<sub>1</sub> contrast enhancer (r<sub>1</sub> = 20.1 mM<sup>-1</sup> s<sup>-1</sup> at 1.4 T) that, when combined with FL, can be used to monitor of the uptake of DOX by cancer cells. This is a straightforward example of a small-molecule based theranostic with environmentally OFF/ON switchable fluorescence capabilities and environmentally activated therapy.

The response mechanisms of the discussed pH-activated theranostics have been summarised in Table 1.

### Redox responsive smart theranostics

The redox potential of neoplastic tissues is distinct from that of healthy tissues and also varies between extracellular and intracellular compartments [133]. γ-L-glutamyl-L-cysteinyl-glycine, or GSH, plays a major role in the maintenance and regulation of the redox status of these tissues [134]. GSH is synthesised in the cytosol and is present there and in subcellular organelles at a 2-10 mM concentration [133, 135]. The concentration of GSH outside cells is much lower (2-10 μM) and this difference can be exploited in the design of smart theranostics. Small-molecule or nanosized theranostic agents can be designed to be highly stable in blood circulation and degrade and release their cargos in the GSH-rich tumour microenvironment or after internalisation in cancer cells. This can be achieved by integrating GSH reduction/oxidation-sensitive bonds in the theranostic agents, such as disulphide (S-S) bonds or reducible amine bonds [136].

**Table 1.** Summary table of the smart theranostics discussed in this section and their pH-responsive mechanisms

Smart theranostic	Structure of responsive linker	Responsive trigger	Responsive Mechanism	Ref
PMN/Ce6		pH	<b>pH = 6.5-7:</b> Ionisation of imidazole groups cause swelling. <b>pH = 5.5:</b> Further ionisation of imidazole groups causes disassembly and release of photosensitiser.	[113]
DOX@ES-MION3@RGD2@mPEG3		pH	<b>pH = 5.5:</b> Cleavage of $\beta$ -propiolate linker leads to exposure of RGD2 ligand and tumour cell internalisation.	[119]
Gd <sub>2</sub> O <sub>3</sub> @MSN-DOX		pH	<b>pH = 5.0:</b> Charge reversal and disintegration of polyelectrolyte P(DMA-co-TPAMA) leads to DOX release.	[115]
MTX-Mn@PEG		pH	<b>pH = 5.5:</b> Protonation of carboxylic acids and nitrogen heterocycle of MTX reduces coordination and releases Mn <sup>2+</sup> from MTX complex.	[117]
SPA-SPIO-IR780		pH	<b>pH = 6.5:</b> Cleavage of bond between PEI and HHPA and exposure of positive amino groups enhances tumour cell internalisation.	[116]
Fe <sub>3</sub> O <sub>4</sub> @TA-PEG/ICG		pH ATP	<b>pH = 5.5:</b> Protonation of hydroxyl groups of TA leads to disassembly by weakening of coordinate and hydrogen bonds. Quenching of ICG is reduced. ATP (10 mM): Displacement of TA from the nanoparticles and disassembly.	[32]
Bi-MSx-PEG/DOX NFs		pH NIR light	<b>pH = 5.5:</b> Solubility of DOX is increased. NIR laser: Temperature increase reduces binding of DOX to NPs, facilitating its release.	[118]
MCDION-Se		pH	<b>pH = 5.5:</b> Degradation of MnCO <sub>3</sub> component of nanoparticles leads to release of Mn <sup>2+</sup> and Se in tumour cells.	[128]

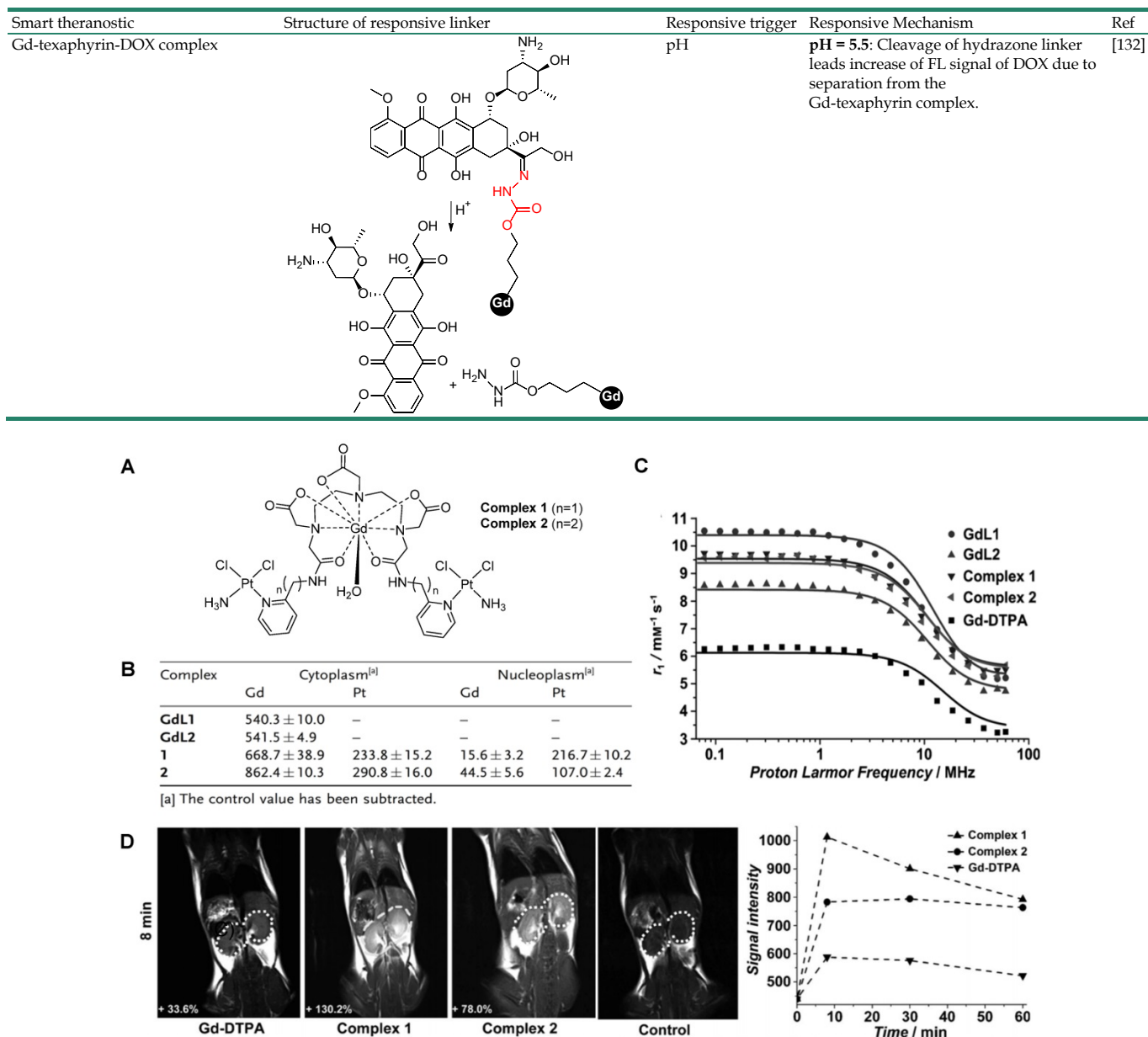


**Figure 7.** **A.** Structure of synthesized theranostic probes 1 and 2. **B.** Cellular uptake of complexes 1 and 2 and Gd-complexes GdL1 and GdL2 (without the platinum moiety) in the cytoplasm and nucleus of HeLa cells measured by ICP-MS. **C.** NMRD profiles of synthesized complexes and Gd-DTPA at different magnetic-field-strengths. **D.**  $T_1$ -weighted MR images of mice at 8 min after the injection of complexes 1 and 2, and Gd-DTPA ( $0.1 \text{ mmol kg}^{-1}$ ), at 3.0 T, and the corresponding MR signal-decay curves. Adapted with permission from [137], copyright 2014 John Wiley and Sons.

Small-molecule theranostics have also been designed to respond to redox agents in the tumour microenvironment. In 2014, Zhu *et al.* reported the synthesis and *in vitro* and *in vivo* validation of a theranostic Gd-Pt probe that could be used to monitor the biodistribution of the platinum-based chemotherapy drug in real time, and presented cytotoxicity values similar to those of cisplatin, even when used at imaging concentrations (Figure 7A) [137]. Since the therapeutic mechanism of platinum complexes mostly involve translocation into the nucleus and binding to DNA, the authors studied the cellular uptake of the theranostic probe in HeLa cells by inductively coupled plasma mass spectrometry

(ICP-MS, Figure 7B). From the results, it is possible to see that the complexes containing a platinum moiety successfully entered cells, as Gd(III) and Pt(II) were both detected in the cytoplasm. Then, complexes 1 and 2 underwent redox-induced dissociation and the platinum moieties migrated and accumulated in the nucleus (Pt:Gd ratio in the nucleoplasm for complex 1 is around 14:1). However, complexes GdL1 and GdL2 did not accumulate in the cytoplasm or nucleus to the same extent, which shows that the platinum moieties may facilitate the cellular uptake of the probe. The relaxivity of the probes was also analysed by proton nuclear magnetic relaxation dispersion (NMRD) and results showed that complexes 1 and 2 ( $r_1 = 6.3 \text{ mM}^{-1}$

$s^{-1}$ ) had higher relaxivity than commercially available Gd-DTPA ( $r_1 = 4.3 \text{ mM}^{-1} \text{ s}^{-1}$ , Figure 7C). This enhancement of the MR signal was also visible *in vivo*, in mice that were injected intravenously with either complex 1, 2 or Gd-DTPA (Figure 7D). Although the *in vitro* results seemed to indicate that complex 2 would accumulate to a higher extent inside cells, the *in vivo* results showed that complex 1 induced a brighter MRI signal in the kidneys, possibly due to different internalisation kinetics *in vivo*. As such, these environmentally responsive chemotherapy complexes could be used to monitor the distribution of platinum drugs and assess their therapeutic response in real time. Other Gd-Pt complexes have been tested as GSH-responsive theranostics for cancer following the same rationale [138, 139].

More recently, a target specific redox-responsive small-molecule theranostic prodrug containing a gadolinium contrast agent was synthesized and biologically tested [140]. This theranostic agent contained: 1) Gd-DOTA as a contrast agent, 2) biotin as a targeting agent that binds to overexpressed biotin receptors in cancer cells, 3) camptothecin (CPT) as an anticancer drug and fluorescent probe, and 4) a disulphide linker that responds to the reductive environment inside cancer cells (Figure 8). The authors performed *in vitro* and *in vivo* studies that

showed that the MRI signal gradually intensified after treatment of A549 cells or mice bearing A549 tumours with the probe.  $T_1$ -weighted images showed that the prodrug selectively bound to tumour cells. Analysis of the tumours' growth also showed that the prodrug was not only being taken up by cancer cells but also that it was being metabolized in response to the reducing environment, thus releasing the anticancer drug specifically inside the tumour. This kind of small-molecule design, although synthetically challenging, has advantages associated with its simplicity, including a better understanding and modulation of the mechanism of drug release and, in some cases, rapid renal clearance. However, its simplicity also makes it difficult to integrate multiple functions in a single agent. Additionally, it might be more challenging to surpass the detectable contrast enhancement threshold, due to the often less efficient tumour cell uptake and accumulation [141]. Alternatively, redox-responsive nanosystems have also been designed with different nanomaterials: mesoporous silica nanoparticles (MSNs) [142, 143], carbon nanomaterials [144, 145], gold nanomaterials [105, 146] and others [133, 147-152]. By incorporating a magnetic component, some of these nanoparticles could be used as MRI theranostics for cancer therapy.

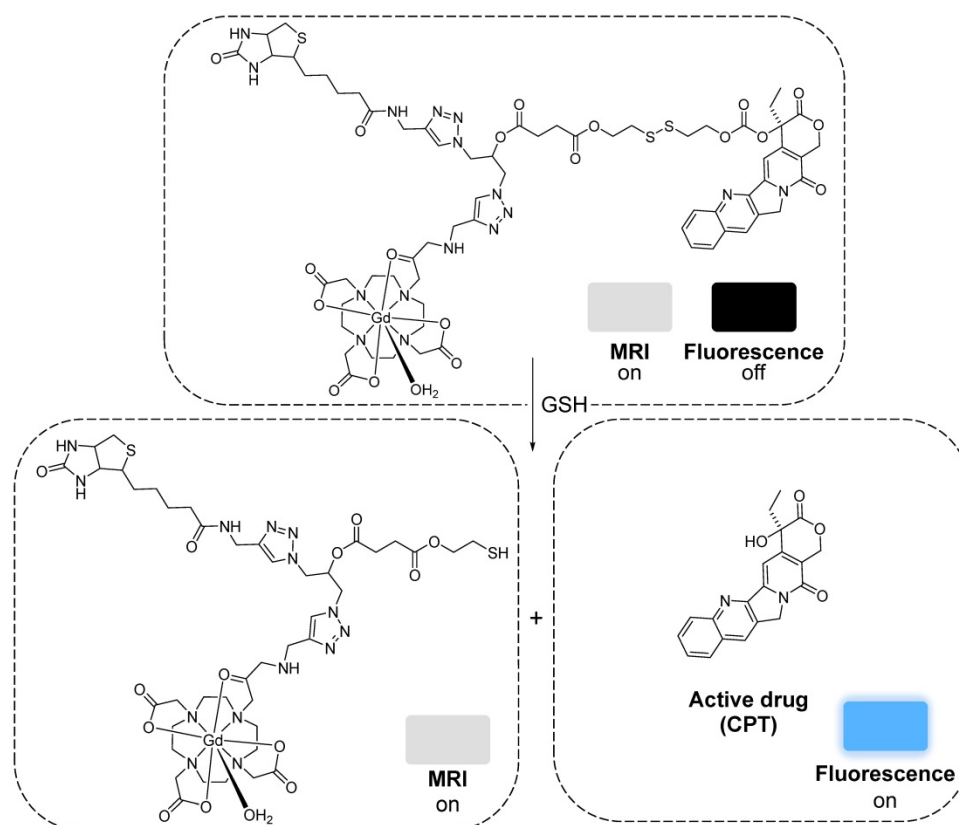


**Figure 8.** The mechanism of the release of CPT from the gadolinium theranostic agent [140].

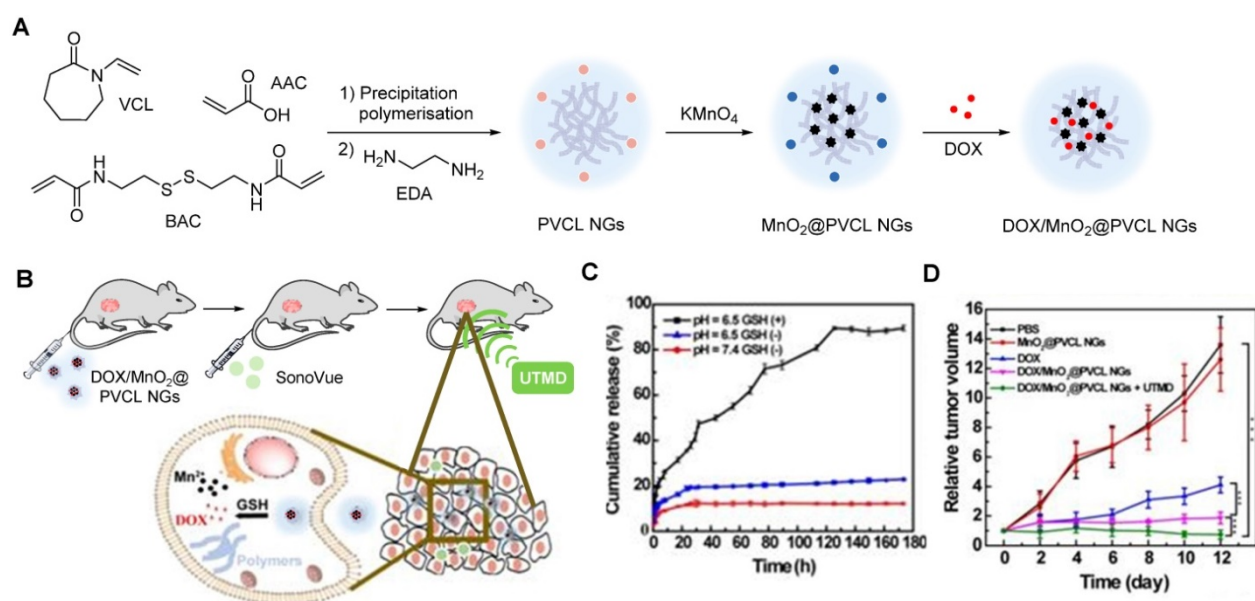


**Figure 9.** A Synthetic route for the fabrication of DOX/MnO<sub>2</sub>@PVCL NGs. B Schematic illustration of the utilization of DOX/MnO<sub>2</sub>@PVCL NGs for UTMD-promoted delivery of NGs for MRI-guided cancer chemotherapy. C DOX release profile from DOX/MnO<sub>2</sub>@PVCL NGs at pH = 7.4 or 6.5 in the presence or absence of GSH (10 mM). D Tumour growth curves after different treatments (n = 5). Tumour volumes were normalized to their initial values. Adapted with permission from [148], copyright 2020 Ilyspring International Publisher.

For example, Zhu *et al.* designed a theranostic system by binding a platinum anticancer prodrug to poly(ethylene glycol) coated Fe<sub>3</sub>O<sub>4</sub> SPIONs (PEG-SPIONs) [147]. The conjugation with PEG molecules ensured that the nanoparticles had improved chemical and colloidal stability, biocompatibility and pharmacokinetics. The use of a cisplatin prodrug, HSpt, improved the cytotoxicity of the system towards cancer cells. Usually, cisplatin is chelated by GSH to form Pt-GS-Pt adducts that are unable to bind to DNA. However, in this case, the authors reported limited Pt(II) detoxification by GSH, as the intermediate adduct Pt-GS, which still retains some DNA binding abilities, was detected at much higher concentrations than Pt-GS-Pt. It was also reported that treatment with these nanoparticles induced depletion of GSH levels of up to 48.7% (for A549 cells). The participation of GSH in the reduction of Pt(IV) to Pt(II) complexes seemed to contribute to the considerable depletion of GSH levels, which resulted in a less efficient detoxification process when compared to cisplatin and thus to an enhanced cytotoxic effect of these Pt(IV) complexes.

Manganese oxide nanoparticles can also be used as redox responsive  $T_1$  contrast agents in nanocarriers. A redox-responsive hybrid nanosystem composed of DOX and poly(N-vinylcaprolactam) (PVCL) co-loaded nanogels (NGs) and with MnO<sub>2</sub> nanoparticles was designed for MRI-guided and ultrasound-targeted microbubble destruction (UTMD) promoted chemotherapy [148]. These DOX/MnO<sub>2</sub>@PVCL NGs were synthesised by a precipitation polymerisation procedure that was followed by loading with MnO<sub>2</sub>

nanoparticles through oxidation with permanganate (Figure 9A). DOX was added *via* physical encapsulation and Mn-N coordination to afford 106.8 nm nanoparticles. The NGs' ability to release DOX in response to redox species like GSH was evaluated. Results demonstrated that after 7 days, only 10% of DOX had been released in a buffer at pH = 7.4 without GSH (Figure 9C). At the same time point, 20% was released in a buffer without GSH at pH = 6.5. Importantly 89.5% of DOX was released from the NGs after 7 days incubation in a medium containing 10 mM of GSH at pH = 6.5. The drug release was potentiated by GSH-mediated cleavage of S-S bonds within the nanogels, which induced swelling of the nanoparticles and freed DOX. The relaxometry of the DOX/MnO<sub>2</sub>@PVCL NGs was also dependent on GSH, since  $T_1$  enhancer Mn<sup>2+</sup> was released in the presence of the redox agent. The  $r_1$  of the NGs increased from 0.04 mM<sup>-1</sup> s<sup>-1</sup> to 8.33 mM<sup>-1</sup> s<sup>-1</sup> at 0.5 T in solutions with 10 mM of GSH ( $r_1$  of Magnevist at 0.5 T is 4.56 mM<sup>-1</sup> s<sup>-1</sup>).  $T_1$ -weighted MRI showed adequate signal enhancement properties for these nanogels. The antitumoral effect of the theranostic systems was evaluated in the presence and absence of UTMD and compared to the efficacy of DOX by itself (Figure 9D). UTMD can be used to enhance chemotherapy since it uses sonoporation to increase tumour capillary permeability and endocytosis. Results showed that the DOX/MnO<sub>2</sub>@PVCL NGs theranostic platforms with environmentally activated therapy and switchable contrast agents, exhibited enhanced therapeutic efficacy when combined with UTMD in comparison to treatment with DOX or NGs only. This type of design,

however, poses the same concerns regarding neurotoxicity of free  $\text{Mn}^{2+}$  ions.

The redox responsiveness of gold nanomaterials has also been explored. Liu *et al.* designed magnetic gold nanowreaths (AuNWs) that could be used for redox-responsive MR, PA and PTT [105]. These nanowreaths were comprised of an inner core of AuNWs surrounded by a layer of silica and a shell of PEG-conjugated ESIONs. The inner core of the nanoparticles was synthesised by Au-nanoring-mediated growth, followed by introduction of a silica shell and then layer-by-layer self-assembly of polymers and ESIONs (Figure 10). Finally, PEG was conjugated to the ESIONs to afford magnetic AuNWs with an overall diameter of 100.7 nm.

These platforms were found to be good PTT effectors and showed interesting MRI properties. When the magnetic nanowreaths were intact, with ESIONs, (usually good  $T_1$  CAs) compacted onto the surface, the overall  $r_1$  of the complex was relatively low ( $r_1 = 1.1 \text{ mM}^{-1} \text{ s}^{-1}$  at 7 T) and the  $r_2$  was high ( $r_2 = 198.6 \text{ mM}^{-1} \text{ s}^{-1}$  at 7 T). This resulted in darker contrast in the MR images, due to the low surface-to-volume ratio of the assembled particles. However, in the presence of GSH (10 mM), the  $r_2$  decreased to  $33.9 \text{ mM}^{-1} \text{ s}^{-1}$  and the  $r_1$  increased, to  $3.2 \text{ mM}^{-1} \text{ s}^{-1}$ , which allowed for a  $T_1$  switch from “on” to “ON” in the presence of GSH. This effect was caused by the cleavage of disulphide bonds in the polymers attached to the silica layer, which allowed for the release of ESIONs from the nanoconstructs that could be observed in TEM images (Figure 10B). The MR images of U87MG tumour bearing mice show that the injection of magnetic AuNWs produces a  $T_1$  signal enhancement, which means that the probe is being cleaved inside GSH-rich tumour cells (Figure 10C). Additionally, the brightest  $T_1$  signal enhancement (2.2 times enhancement when compared to pre-injection signal) of magnetic AuNWs occurs after 24 h, while Magnevist and ESIONs induce maximum enhancement of 1.8 and 1.7 times the pre-injection signal at 1 and 4 h, respectively. PA was also used and confirmed that the signal enhancement gradually increases until 24 h post injection (Figure 10D). This work also shows that these magnetic AuNWs allowed for the effective removal of subcutaneous tumours through PTT, since the gold branches, small junctions, and central holes of the nanowreaths improved the absorbance and photothermal properties of the gold nanoconstructs (Figure 10E). This is then an example of a multifunctional and multimodal theranostic that combines remotely activated therapy with environmentally switchable imaging agents that show a distinct contrast enhancement in GSH-rich tumour cells.

Photosensitiser nanoassemblies (NP-RGDs) have also been reported as GSH and light-responsive dual modal MRI/FL theranostic platforms for PDT [153]. These nanoparticles were prepared *via* self-assembly of an NIR photosensitiser pheophorbide (PPa) for FL and PDT, a GSH-cleavable linker, a fluorophore to facilitate self-assembly, a paramagnetic Gd-DOTA chelate for MRI and a cyclic RGD peptide for  $\alpha_v\beta_3$  targeting. *In vivo* studies showed that the NP-RGD nanoparticles worked as  $T_1$  contrast agents ( $r_1 = 20.0 \text{ mM}^{-1} \text{ s}^{-1}$  at 0.5 T) and selectively accumulated in U87MG tumours, leading to a 61% signal enhancement in tumours 2 h after injection, a 9-fold increase when compared to untargeted nanoassemblies. Following entry into tumour cells, the disassembly of the nanoparticles, which had quenched fluorescence and PDT abilities, was triggered by disulphide reduction by GSH. A fluorescent product and PPa-SH, a hydrophobic photosensitiser, were then formed and the fluorescence at 547 nm was increased by 77-fold, which translated into the FL images. PPa-SH was then bound to endogenous albumin, which afforded prolonged retention in tumours, more efficient  $^1\text{O}_2$  generation for PDT, and consequently more efficient ablation of tumours.

Lin *et al.* designed GSH-responsive MRI theranostics that could be used for CDT [154]. Since the efficiency of CDT is diminished by the elevated levels of detoxifying molecules like GSH present in tumour microenvironments or cancer cells, these researchers designed  $\text{MnO}_2$ -functionalised mesoporous silica nanoparticles (MS@ $\text{MnO}_2$  NPs) with GSH depletion properties. These theranostics had environmentally switchable imaging abilities, as the  $r_1$  of the nanopatforms increased 13-fold upon GSH-mediated release of  $\text{Mn}^{2+}$  ions from the NPs' shell. This OFF/ON switch was also observable *in vivo* in  $T_1$ -weighted images, where a significant contrast enhancement was observed in U87MG tumours up to 24 h post injection of the MS@ $\text{MnO}_2$  NPs. *In vivo* studies were also used to evaluate the CDT efficiency of the theranostic platforms and showed that tumour growth was significantly suppressed, but not inhibited, after injection with the NPs. Modified CPT-loaded nanoparticles (MS@ $\text{MnO}_2$ -CPT NPs) were also tested and displayed tumour growth inhibition at a reduced Mn dose. This example suggests once more that CDT on its own can decrease tumour growth rates, but it is in combination with other treatment modalities where CDT shows the most promising effects.

The response mechanisms of the discussed pH-activated theranostics have been summarised in Table 2.

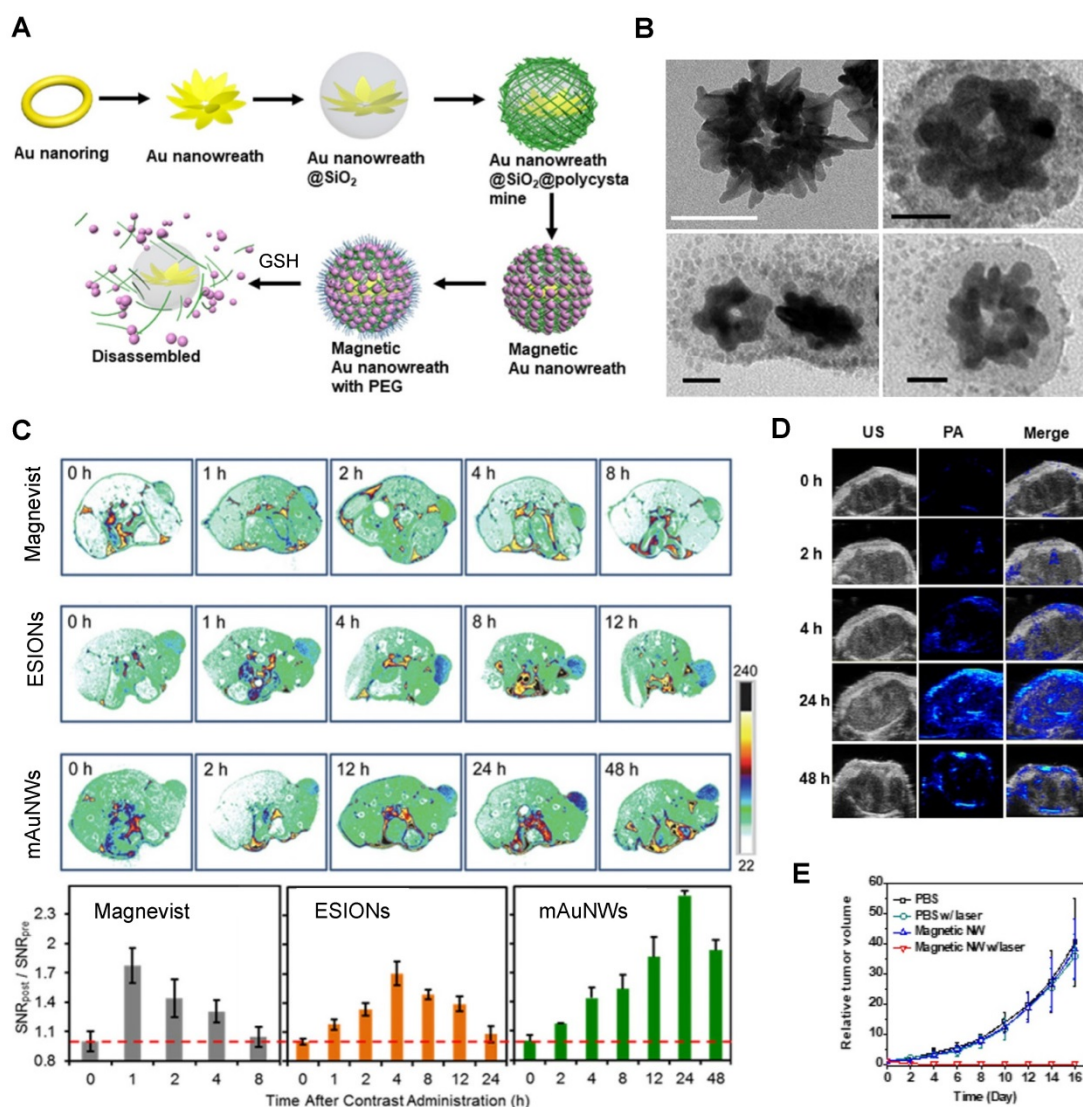


**Figure 10.** **A** Schematic illustration of the synthesis of magnetic gold nanowreaths. **B** Representative TEM images of AuNWs (top left), magnetic AuNWs before incubation with GSH (top right), magnetic AuNWs after 30 min incubation with 10 mM GSH (bottom left) and magnetic AuNWs after 2 h incubation with 10 mM GSH (bottom right); scale bar: 50 nm. **C**  $T_1$ -weighted images of U87MG tumour-bearing nude mice and corresponding quantification of the tumour signals after intravenous injection of 5.0 mg/kg of Magnevist, ESIONs or magnetic AuNWs. The signal enhancement in tumours for different contrast agents at different time points after injection were quantified as the division of signal-to-noise ratio (SNR) of tumours at different time points post injection by the SNR of tumours at 0 h. **D** *In vivo* PA and PTT with magnetic AuNWs showing US, PA, and merged images of tumour before injection and at 2, 4, 24, and 48 h after intravenous injection of magnetic AuNWs upon irradiation by an 808 nm pulsed laser. **E** Relative tumour volume after different treatments and irradiation with an 808 nm CW laser at 0.75 W cm<sup>-2</sup>. Adapted with permission from [105], copyright 2018 American Chemical Society.

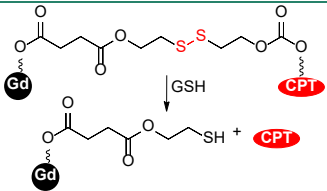
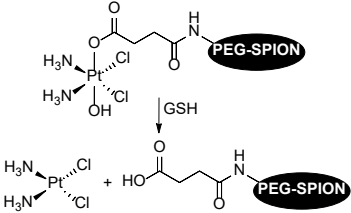
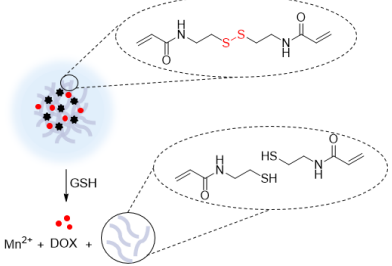
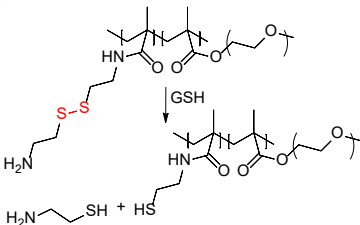
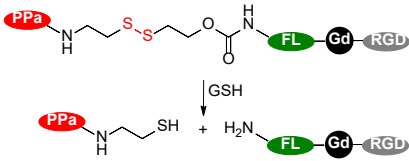
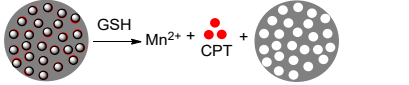
## Enzyme responsive smart theranostics

Enzyme-responsive theranostics have also been explored, to take advantage of the altered expression levels of enzymes in pathological conditions, including cancer [155]. Researchers have been interested in using enzymes as an endogenous stimulus for drug release because enzymatic reactions are fast, highly efficient, and very specific and selective. Different theranostic agents have been designed to respond to matrix metalloproteinases (MMPs) [156], cathepsins [157, 158], cysteine caspases, phospholipases, or hyaluronidases, for example [29, 159].

Santra *et al.* developed a convenient methodology that allowed for the synthesis of an

esterase-sensitive theranostic agent [160]. The method included co-encapsulation of an anticancer drug, taxol, and NIR dyes inside hydrophobic pockets of a polyacrylic acid (PAA) coated SPION. This complex was further modified by “click chemistry” to include folate as a targeting agent towards cancer cells. These nanoparticles selectively released taxol and NIR dyes in an esterase-dependent manner or in acidic conditions. Although the mechanism by which the nanosystems release taxol in response to the enzyme is not fully elucidated, this could be an easy and scalable strategy to synthesize targeted theranostics with enzyme activated therapy and switchable fluorescence signals.

**Table 2.** Summary table of the smart theranostics discussed in this section and their redox-responsive mechanisms

Smart theranostic	Structure of responsive linker	Responsive trigger	Responsive Mechanism	Ref
Gd-DOTA-Biotin-CPT complex		Redox	GSH (5 mM): Cleavage of disulphide linker causes release of CPT and an increase in FL signal intensity.	[140]
HSPt-PEG-SPION		Redox	GSH (2 mM): Reduction of Pt(IV) complex to a Pt(II) species causes dissociation of HSPt-PEG-SPIONs and release of active drug cisplatin.	[147]
DOX/MnO <sub>2</sub> @PVCL NGs		Redox	GSH (10 mM): Cleavage of disulphide bonds within nanogel polymers and decomposition of MnO <sub>2</sub> nanoparticles to Mn <sup>2+</sup> ions lead to the release of DOX and increase of the MR signal.	[148]
Magnetic AuNWs		Redox NIR light	GSH (10 mM): Cleavage of disulphide bonds in polymers induces disassembly of AuNWs and release of ESIONs.	[105]
NP-RGD		Redox NIR light	GSH (10 mM): Cleavage of disulphide and disassembly of NP-RGD nanoparticles.	[153]
MS@MnO <sub>2</sub> -CPT NPs		Redox	GSH (10 mM): Decomposition of MnO <sub>2</sub> nanoparticles to Mn <sup>2+</sup> ions and subsequent release of previously blocked CPT from MS NPs.	[154]

Lee *et al.* also synthesised a SPION-based enzyme-sensitive MRI theranostic agent, in this case responsive to cathepsin B [157]. They engineered urokinase plasminogen activator receptor (uPAR)-targeted magnetic iron oxide nanoparticles (IONPs) that delivered chemotherapy drug gemcitabine (Gem) to uPAR-expressing tumour and stromal cells, such as pancreatic cancer cells. These ATF-IONP-Gem nanoconstructs were prepared by conjugation of the targeting vector, an amino-terminal fragment (ATF) peptide of the receptor-binding domain of natural ligand uPA, to the IONPs. Gem was also conjugated to the nanoparticles through a tetrapeptide linker that can be cleaved by lysosomal

cysteine protease, cathepsin B, which is overexpressed in pancreatic cancer cells (Figure 11A). HPLC analysis showed that the release of Gem from these nanoconstructs was dependent on the presence of cathepsin. Indeed, these studies showed that 82% of Gem was released from ATF-IONP-Gem nanoparticles in response to cathepsin and in mildly acidic conditions (pH = 5.5). MIA PaCa-2 tumour-bearing mice were treated with 2 mg kg<sup>-1</sup> of Gem alone, non-targeted IONP-Gem or ATF-IONP-Gem twice per week, for a total of five times. The antitumor effect of these treatments was evaluated *in vivo* and results showed that ATF-IONPs led to 50% tumour growth inhibition, which is higher

than the inhibition observed after injection with Gem or IONP-Gem, 23% and 30%, respectively. This implies that the use of the targeting agent positively affects the therapeutic outcome.

This targeted delivery was imaged using  $T_2$ -weighted MRI. These nanoplatforms present a  $r_2$  of  $195 \text{ mM}^{-1} \text{ s}^{-1}$  at 3 T, which is much higher than that of Endorem® ( $45 \text{ mM}^{-1} \text{ s}^{-1}$  at that field strength) [161]. *In vivo* MR images (Figure 11B) show that the targeted theranostic agents contributed to a decrease of 24% in the MRI signal at the tumour site following systemic delivery, which makes it possible to image drug delivery and accumulation in cancerous tissues. The accumulation of ATF-IONP-Gem nanoparticles was also confirmed by histological studies, which show specific accumulation of the targeted theranostic platforms in tumours, while no significant accumulation in healthy tissues was observed

(Figure 11C).

Cai *et al.* also designed a cathepsin B-sensitive theranostic agent, but it was small-molecule polymer-based. They prepared novel amphiphilic biodegradable conjugates, pHPMA-Gd-PTX-Cy5.5, made of a gadolinium chelate as a  $T_1$  MRI agent, chemotherapy drug paclitaxel (PTX), fluorescence dye cyanine 5.5 (Cy5.5) and a cathepsin B-sensitive GFLG peptide (Figure 12A) [158]. First, a pHPMA-DOTA-PTX copolymer was synthesised by a two-step reversible addition-fragmentation chain transfer (RAFT) polymerization. These copolymers were then labelled with Cy5.5 through a click reaction, which was followed by a complexation reaction between  $\text{Gd}^{3+}$  and the DOTA chelators. This afforded pHPMA-Gd-PTX-Cy5.5 as 92 kDa nanoparticles after hydrophobic interaction-induced self-assembly of the polymers. The release of PTX from the conjugates was

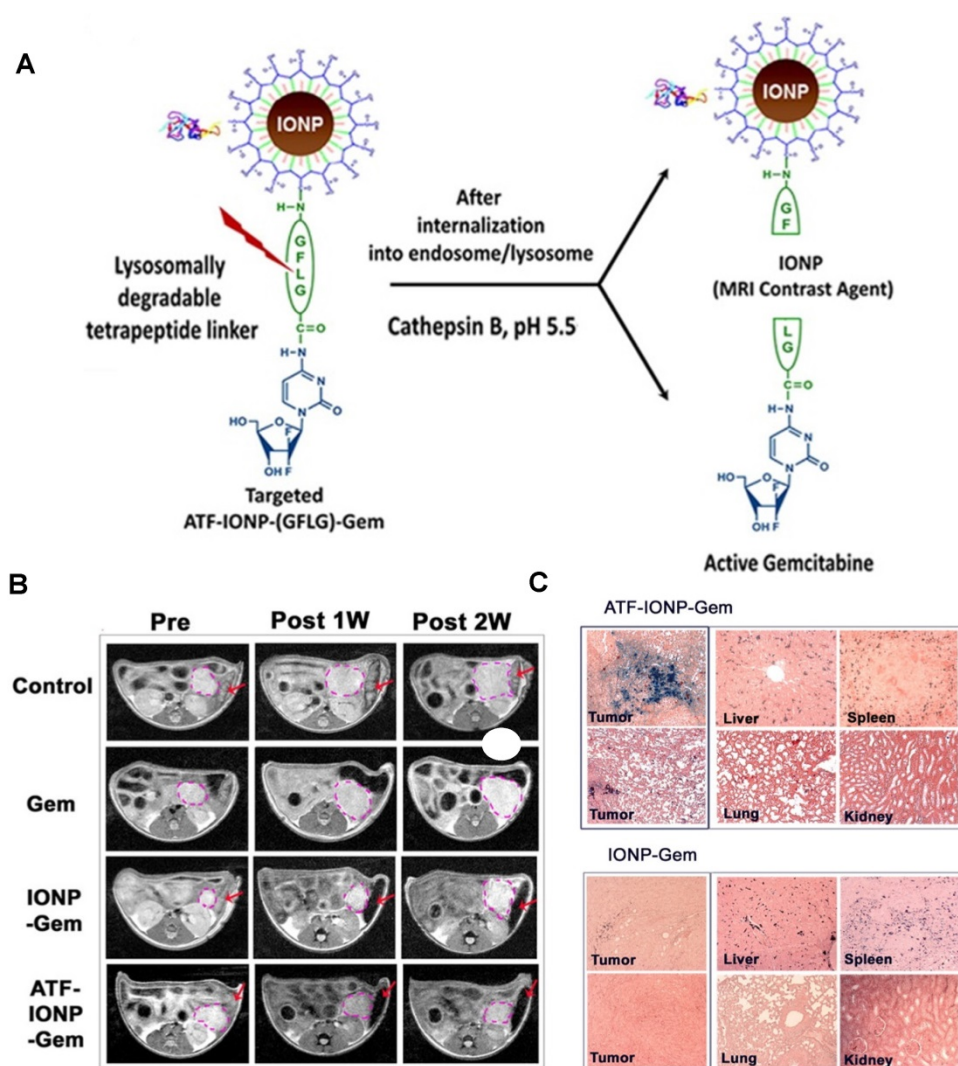


**Figure 11.** A. Schematic diagram of Gem release from ATF-IONP-Gem. B. Axial  $T_2$ -weighted MR images of the tumour-bearing mice before and one week and two weeks after receiving theranostic nanoparticles, at 3.0 T. Post-treatment images were obtained 48 h following the second (1 week) and fourth (2 weeks) injection. The location and size of the cancer lesions (pink dotted circles) can be seen in the MR images. Red arrows indicate the MRI contrast change in the spleen. C. Biodistribution of ATF-IONP-Gem and non-targeted IONP-Gem following systemic treatments. Tumour and normal tissue sections obtained from mice at the end of the five treatments were stained with Prussian blue staining. Blue: IONP positive cells; red: Nuclear Fast Red background staining. Adapted with permission from reference [157], copyright 2013 American Chemical Society.

evaluated with reverse phase HPLC, in the presence and absence of cathepsin B, at different pH values (Figure 12B). Results showed that up to 90% of PTX was released within 24 h in a medium containing cathepsin B (2.8  $\mu\text{M}$ ) at pH = 5.4, which was much higher than the release of PTX without the lysosomal enzyme (20% release after 24 h). The nanoparticles were also evaluated as  $T_1$  MRI contrast agents. The pHPMA-Gd-PTX-Cy5.5 constructs had  $r_1 = 12.9 \text{ mM}^{-1} \text{ s}^{-1}$  at 1.5 T, which was significantly higher than the relaxivity of commercial Gd-DTPA at that magnetic field strength ( $2.4 \text{ mM}^{-1} \text{ s}^{-1}$ ). The high efficiency of these nanoparticles as MRI CAs was also observed during *in vivo* MRI of mice bearing 4T1 breast carcinoma xenografts, at 3 T (Figure 12C). When compared to Gd-DTPA, pHPMA-Gd-PTX-Cy5.5 platforms exhibited a more gradual but more intense signal increase at the tumour site that lasted up to 24 h after injection. This showed that the nanoparticles have extended blood circulation and accumulate preferentially at tumour sites. ICP-MS studies indicated that the nanoparticles' route of excretion mainly involved the liver and spleen, since there was an accumulation of 26% and 13% per gram, respectively, in these organs after 24 h, which decreased to 11.4%  $\text{g}^{-1}$  and 3.5%  $\text{g}^{-1}$  at 96 h post injection. The pHPMA-Gd-PTX-Cy5.5 conjugate based nanoparticles provided significantly enhanced antitumoral properties, since they inhibited tumour growth by 95.5% on average (Figure 12D) versus only 16.7% of free PTX. This is a successful example of how

small molecules can be conjugated into a larger polymer-based nanoparticle with enhanced blood circulation, enzyme-responsive drug release mechanism, increased efficacy as a  $T_1$  contrast agent and improved anticancer properties.

Recently, the same group of researchers designed a similar stimuli-responsive polymeric nano-agent with enhanced MR, fluorescence and antitumoral efficacy following the same rationale [28].

Shi *et al.* designed an MMP-2 activated Gd-doped CuS nanoprobe (T-MAN) that could be used for dual modal MR/FL imaging of gastric tumours [162]. The nanoparticles were formed by covalent modification of Gd-doped CuS micellar nanoparticles with a cRGD peptide and an MMP-2-cleavable fluorescent substrate. These nanoplatforms had high relaxivity values ( $60 \text{ mM}^{-1} \text{ s}^{-1}$  per Gd at 1 T), which, coupled with the dual targeting strategies employed in the NPs (targeting of  $\alpha_v\beta_3$  integrins through RGD peptide and targeting of tumour microenvironment *via* addition of an MMP-2 substrate), resulted in the highest uptake of T-MAN in gastric tumours 12 h post injection ( $\sim 23.4\% \text{ ID\% g}^{-1}$ ) and translated in a significant  $T_1$  signal enhancement. The efficiency of these platforms as PTT effectors was also tested in MKN45/Luc gastric-tumour bearing mice. T-MAN nanoparticles had a high photothermal conversion efficiency (70% following treatment with 808 nm laser,  $0.85 \text{ W cm}^{-2}$  for 10 min). Exposure of mice to a 808 nm laser after injection of T-MAN theranostics led to a more significant temperature increase in the stomach of

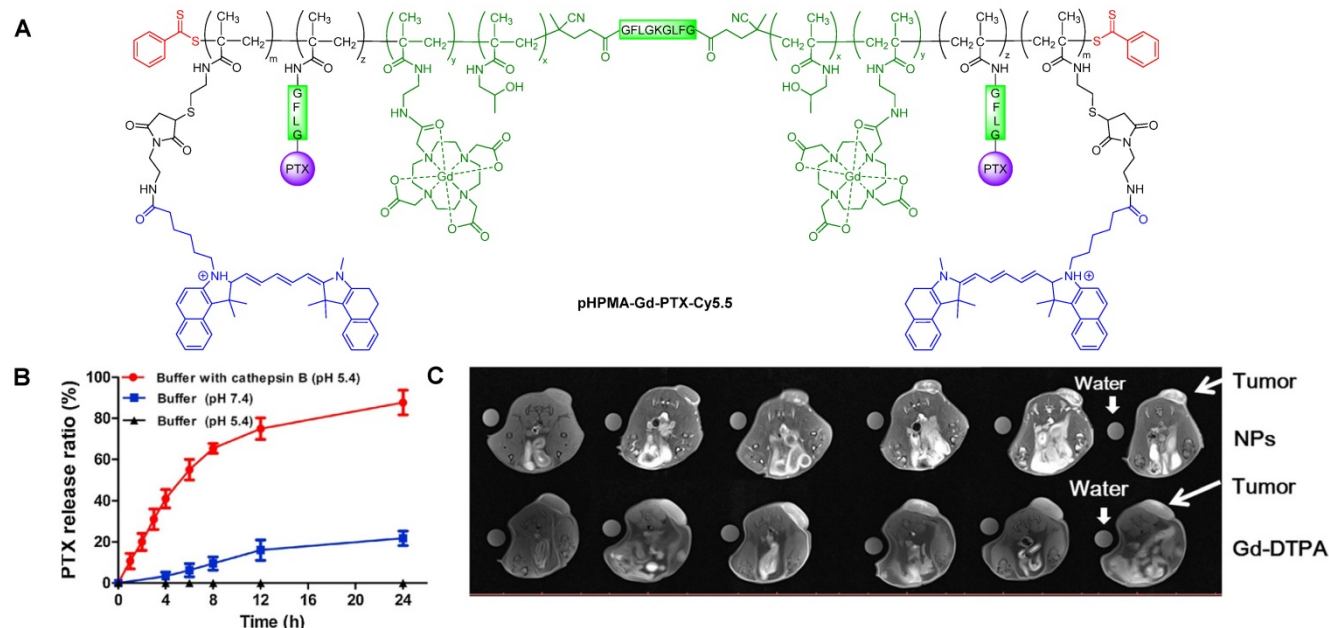


**Figure 12.** A. Structure of pHPMA-Gd-PTX-Cy5.5 conjugate. B. *In vitro* drug release profiles of PTX-conjugated nanoparticles after incubation in pH = 5.4 McIlvaine's buffer with cathepsin B (2.8  $\mu\text{M}$ ), pH = 5.4 McIlvaine's buffer without cathepsin B, and pH = 7.4 PBS without cathepsin B at 37 °C. C. MR axial imaging of tumours in tumour-bearing mice intravenously injected with Gd-DTPA or nanoparticles at predetermined time points (0.08 mmol Gd(III)  $\text{kg}^{-1}$  mouse), at 3.0 T. Adapted with permission from reference [158], copyright 2018 Elsevier.



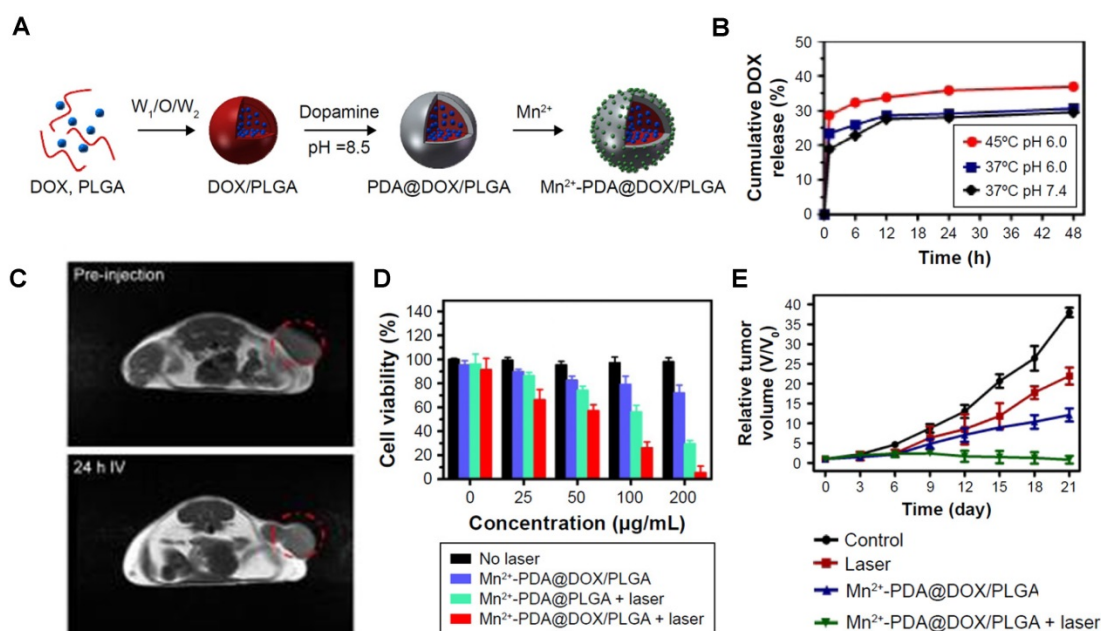


**Figure 13.** **A** Schematic diagram of synthesis process of Mn<sup>2+</sup>-PDA@DOX/PLGA nanoparticles. **B**. DOX release percentage from Mn<sup>2+</sup>-PDA@DOX/PLGA at varied pH values and temperatures. **C**. *In vivo* T<sub>1</sub>-weighted MR images of a mouse taken before injection (upper) and 24 h post intravenous injection (bottom) with Mn<sup>2+</sup>-PDA@PLGA, at 3.0 T. The red circle is the tumour region of the mice. **D**. Relative viabilities of CT26 cells incubated with various concentrations of Mn<sup>2+</sup>-PDA@PLGA and Mn<sup>2+</sup>-PDA@DOX/PLGA nanoparticles with or without an 808 nm laser irradiation (1.0 W cm<sup>-2</sup>) for 10 min. **E**. Tumour growth curves of different groups after treatment. The tumour volumes were normalized to their initial sizes. Adapted with permission from [35], copyright 2017 Dove Medical Press.

The release of DOX was analysed by UV-vis spectroscopy and inductively coupled plasma atomic emission spectroscopy (ICP-AES) and showed that the drug release is triggered by increased temperature originating from the absorption of a NIR light by PDA (Figure 13B). As such, this theranostic platform could be considered light responsive, and not temperature responsive, but it was classified as the latter since the drug release is potentiated by the temperature increase, which causes the loosening of the PLGA mesh, not by the laser irradiation itself. *In vivo* T<sub>1</sub>-weighted MR images show a slight contrast enhancement 24 h post injection with the Mn<sup>2+</sup>-PDA@PLGA nanoparticles, due to the presence of Mn<sup>2+</sup> ions on the surface and accumulation at target sites (Figure 13C). The therapeutic efficacy of these particles was confirmed in *in vitro* and *in vivo* assays, which showed a synergic effect between chemotherapy and PTT when mice were exposed to an 808 nm laser following treatment with DOX-loaded nanoparticles (Figure 13D and E).

Recently, de Moura *et al.* presented the design, preparation, and proof-of-principle validation of novel magnetic hybrid nanowax composites, mWNVs, as temperature responsive MRI and chemotherapy/MH theranostic agents (Figure 14A) [41]. These *Carnauba* wax spherical nanoparticles incorporated 8 nm magnetic nanoparticles and chemotherapy drug Oncocalixone A (Onco A) and were synthesised by a simple and scalable modified

melt emulsification protocol and loaded with 0-7% iron oxide nanoparticles in respect to wax (w/w). These platforms showed very promising results for T<sub>2</sub>-weighted MRI, since the *r*<sub>2</sub> for compound S7 (7% MNPs) was 930 mM<sup>-1</sup> s<sup>-1</sup> at 1.4 T, which is much higher than the relaxivity of commercially available Endorem at that magnetic field strength (61 mM<sup>-1</sup> s<sup>-1</sup>). The efficiency of mWNVs as MH effectors was also evaluated. All the magnetite-loaded samples showed high specific absorption rates (SAR) values >220 W g<sup>-1</sup> Fe, therefore S7 was chosen for drug loading because it showed the largest *r*<sub>2</sub> of all the tested compounds. After Onco A loading into the wax nanocomposites, the drug release mechanism was studied using fluorescence measurements. Results showed that the chemotherapeutic drug release was enhanced in S7-Onco A nanocomposites in response to the temperature increase resulting from the application of a 24 mT (523 kHz) alternating magnetic field (Figure 14C and D). *In vitro* studies indicated a synergistic effect between thermo and chemotherapy, which is expected, since the drug release is a diffusive process that depends on heat generation and MH has been known to sensitise tumour cells to chemotherapy, in addition to direct thermal ablation. This proof-of-concept work takes a step forward in the design of highly controllable organic/inorganic lipid-based nanotheranostics and it is relevant for the design of future externally triggered drug release systems with integrated imaging.

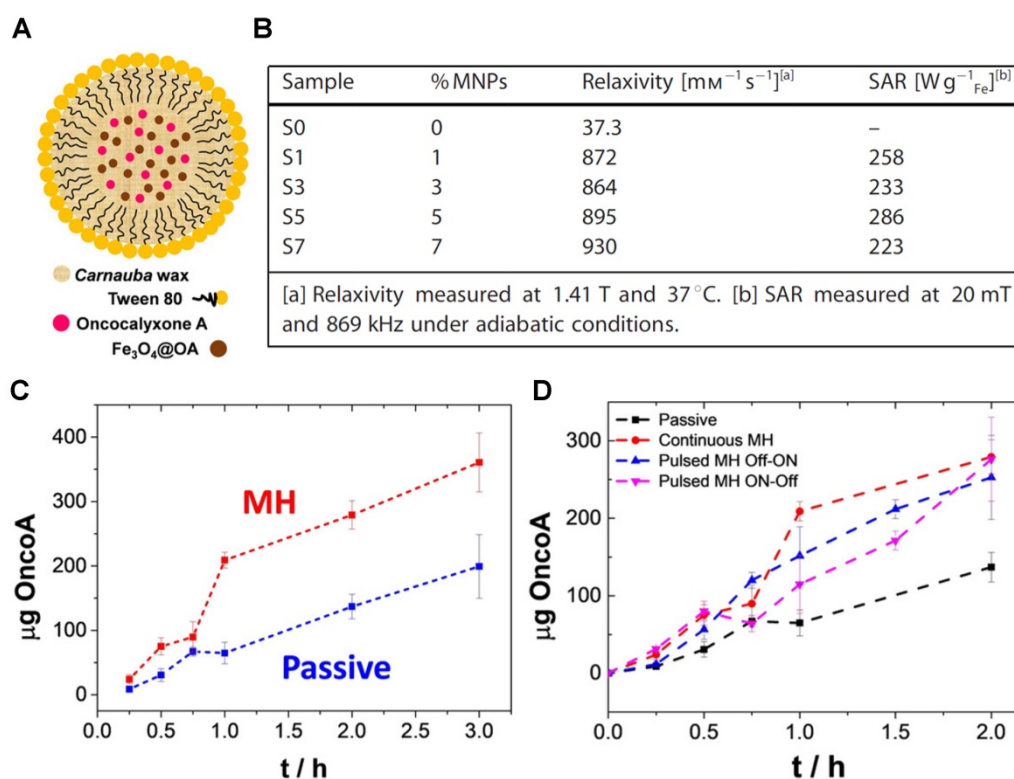


**Figure 14.** **A.** Schematic representation of the mWNVs. **B.** Relaxometric and MH properties of the mWNVs. **C.** Comparison of passive versus MH-induced release (24 mT and 523 kHz, 2 h) of Onco A from S7-Onco A during the first 3 h. **D.** Comparison of the cumulative release of Onco A from S7-Onco A under different conditions: black, room temperature passive release; red, continuous MH-induced release; blue, pulsed Off-ON MH-induced release; pink, pulsed ON-Off MH-induced release. Adapted with permission from reference [41], copyright 2020 John Wiley and Sons.

### Ultrasound responsive smart theranostics

Ultrasounds are high frequency sounds waves with adjustable intensities for different applications, including imaging (< 20 kHz) or disruption of nanocarriers to trigger the release of encapsulated drugs or MRI CAs (> 20 kHz) [33].

Ultrasounds can also be used for therapy; high intensity focused ultrasound (HIFU) is a non-invasive therapeutic modality that focuses ultrasound waves to induce thermal ablation in tumours [165]. HIFU has also been used to trigger the temperature-dependent generation of microbubbles in PFH/DOX@PLGA/Fe<sub>3</sub>O<sub>4</sub>-FA nanocomposites and thus serve as a MRI/US-guided HIFU/chemo synergistic therapy [166]. These nanotheranostic agents were prepared by a double emulsion method and had DOX encapsulated in a temperature-responsive perfluorohexane (PFH) core and Fe<sub>3</sub>O<sub>4</sub> nanoparticles in a PLGA shell. Folic acid was then added to the outer surface of the nanocomposites *via* carbodiimide reaction. *In vivo* studies were performed in hepatocellular tumour-bearing mice to evaluate the efficiency of these platforms as MRI CAs, US-imaging enhancers, HIFU sensitisers, chemotherapy agents and hyperthermia effectors. *In vitro* studies showed that exposure to HIFU generated a thermal effect that

triggered PFH vaporisation of the NPs with around 49% efficiency. This translated into enhanced *in vivo* US imaging, as the echo enhancement and grey volume increased significantly after exposure to HIFU (5.91 to 128.1). The targeted nanocomposites could also be used for MRI, since they actively accumulated at tumour sites, with the highest contrast enhancement reached at 6 h post injection. The *in vivo* synergistic effect of the PFH/DOX@PLGA/Fe<sub>3</sub>O<sub>4</sub>-FA nanocomposites for HIFU/chemotherapy was then assessed. Treatment with the nanoplateforms led to significant tumour ablation, in comparison to untargeted nanocomposites, or injection of nanoparticles without HIFU exposure. This indicates that these theranostic agents responded to a HIFU stimulus and thus induced the release and increased the susceptibility towards anticancer drug DOX. PFH/DOX@PLGA/Fe<sub>3</sub>O<sub>4</sub>-FA nanocomposites are then examples of smart theranostics with remotely activated US imaging and HIFU/chemotherapy.

Rizzitelli *et al.* developed liposomes that released DOX and MRI CA Gadoteridol in response to pulsed low intensity non-focused ultrasounds (pLINFU) [167, 168]. pLINFU are acoustic waves with intensity lower than 10 W cm<sup>-2</sup> and US frequencies lower or within the therapeutic range (20 kHz-3 MHz) that allow for the release of nanocarriers' cargo through mechanical

interactions, in a process that does not induce a temperature shift. These Gado-Doxo-Lipo liposomes were prepared by hydration of a thin lipid film and yielded nanoparticles with Gadoteridol and DOX encapsulated in a ratio of 11:1, which could help increase the local  $T_1$  signal [167]. *In vivo* studies on a syngeneic mouse model of breast cancer showed that the release and accumulation of DOX and Gadoteridol in tumours was triggered by a single treatment with pLINFU (3 MHz, total insonation time 2 min), as the generated waves induced the permeabilization of the tumour's vascular endothelium. Since Gadoteridol was released simultaneously to DOX, MRI was used to both confirm drug delivery to tumours and to assess the efficacy of the chemotherapy. These researchers then tested these liposomes in a mammary carcinoma model in BALB/C mice using a modified method where two sequential pLINFU shots were applied: the first to release the cargo from liposomes circulating in tumour blood vessels, and the second to increase tumour vessel permeability and thus facilitate the extravasation of the released cargo to tumour cells. This method once again allowed for the evaluation of the cargo release efficiency, as this process was accompanied by an MRI  $T_1$  contrast enhancement in tumours and led to complete regression of the tumours. These liposomes are examples of US-responsive theranostics for MRI with remotely activated therapy.

### Light responsive smart theranostics

Using light as a stimulus has various advantages, including minimal invasiveness and the possibility to easily tune to a desired wavelength and induce a response in a specific system [169, 170]. Light absorption by one or several moieties of the theranostic agents could induce photochemical reactions in those components to trigger drug release, and/or potentiate the interaction of photosensitisers with oxygen to generate singlet oxygen [171]. Absorption of light by these molecules can also be used to facilitate PA or FL imaging, or to improve the therapeutic outcome, through PDT or PTT. Several light-sensitive theranostic agents have been proposed [36-40, 172].

Kim *et al.* used a light source to enhance the generation of singlet oxygen by photosensitiser Ce6 [172]. To do this, they developed Ce6-loaded manganese ferrite nanoparticle-anchored mesoporous silica nanoparticles (MFMSN-Ce6s) that function as theranostic agents for MRI-guided PDT. The nanoparticles work as Fenton catalysts that continuously generate oxygen under hypoxic conditions, which improves the ROS generation of photosensitisers in response to a 680 nm laser [173],

thus enhancing the therapeutic effects of PDT. In terms of synthesis, 6 nm manganese ferrite nanoparticles were conjugated to 50 nm mesoporous silica nanoparticles by a nucleophilic substitution reaction, which was followed by functionalisation with PEG.

These nanoparticles had a hydrodynamic size below 100 nm and an  $r_2 = 60.9 \text{ mM}^{-1} \text{ s}^{-1}$  at 3 T. Ce6 was then loaded on the porous surface of the nanoplateforms. The Fenton catalytic efficiency of MFMSN-Ce6 was evaluated in time-dependent assays that measured the degradation of  $\text{H}_2\text{O}_2$  and the generation of  $\text{O}_2$  under hypoxia conditions (Figure 15A and B). These nanoparticles were able to degrade the former molecule and generate the latter. The ability of Ce6 and MFMSN-Ce6 nanoconstructs to generate singlet oxygen species in response to a 680 nm laser (5 min) under normoxic and hypoxic conditions was also evaluated (Figure 15C). In non-hypoxia conditions, Ce6 and MFMSN-Ce6s were able to produce similar amounts of singlet oxygen. However, under hypoxia conditions, the nanoparticles produced 2.2 times more singlet oxygen in response to the laser. This effect translated into a higher therapeutic efficiency in hypoxia conditions during *in vitro* and *in vivo* studies. MTS assays showed that treatment with Ce6 and MFMSN-Ce6 had a similarly high PDT efficacy in U-87MG cells after laser irradiation under normoxic conditions (Figure 15D). However, in hypoxic conditions, the cell viability only decreases significantly in MFMSN-Ce6-treated cells (Figure 15E). *In vivo* studies showed a significant decrease in tumour volume after irradiation of tumour sites with a 670 nm laser (0.88 W, 5 min, 24 h post treatment) following injection of U-87MG tumour-bearing mice with MFMSN-Ce6 nanoparticles (Figure 15F), due to a higher accumulation of the theranostic agent at the tumour site and enhanced PDT effect under hypoxia conditions. The accumulation of MFMSNs in the tumour region was confirmed by  $T_2$ -weighted MRI, which demonstrated higher signal attenuation at tumour site (Figure 15G).

CuS-MnS<sub>2</sub> nanoflowers were designed as light-enhanced MRI-guided PTT/PDT agents [40]. These nanoparticles showed good photothermal, photostability and photodynamic properties and had a light-to-heat efficiency of 67.5%. This was the first report of Cu-Mn-S nanomaterials boasting NIR light-responsive ROS generation, which accounted for their potent light-dependent anticancer efficacy in the treatment of A2780 tumour-bearing mice. The same principle was applied later for other Mn-based MRI-guided PTT theranostic agents [37].

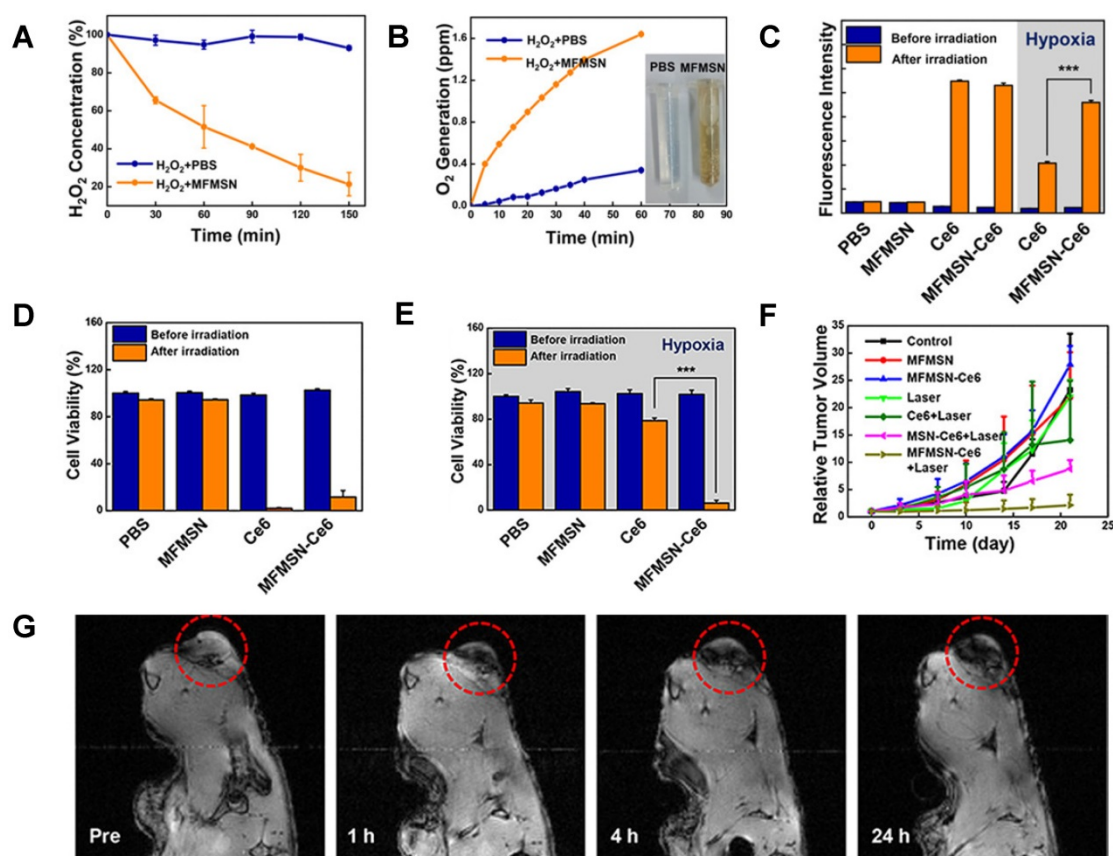


**Figure 15.** A. Degradation of H<sub>2</sub>O<sub>2</sub> (n = 3) and B O<sub>2</sub> generation after treatment with MFMSNs in PBS. C. Generation of singlet oxygen measured by the fluorescence intensity of SOSG (n = 3). D. Cell viability assay of MFMSN-treated U-87MG cells in normoxic environments. E. Cell viability assay of MFMSN-treated U-87MG cells in hypoxic environments. F. Tumour volume changes after treatment of U-87MG tumour-bearing mice. G. *In vivo* T<sub>2</sub>\*-weighted MR images of a tumour-bearing mouse at various time periods, at 9.4 T. Tumours are circled with red dashed lines. Adapted with permission from [172], copyright 2017 American Chemical Society.

Wang *et al.* synthesised folate receptor targeted MRI theranostic nanocapsules, DOX-ICG@Fe/FeO-PPP-FA, for NIR light and tumour microenvironment-responsive PDT and chemotherapy [106]. Interestingly, exposure of these particles to NIR light and acidic pH (pH = 6.5) induce drug release through a novel size-switchable mechanism. This is an example of how light absorption can trigger physical changes that allow for the release of encapsulated components from the theranostic agent. First, by tethering PLGA-polyethylene glycol-poly(N-isopropyl acrylamide), or PPP, to the iron nanoparticles, Fe/FeO-PPP heterostructures were synthesised. Chemotherapy agent DOX and photosensitiser ICG were then co-loaded into the Fe/FeO-PPP structures by water-oil-water emulsion (Figure 16A).

These nanoparticles had large average sizes (219 ± 52 nm), which might contribute to a longer blood circulation half-life but could hinder their ability to extravasate to tumour tissues [174, 175]. In this work, a size-switchable strategy was employed to not only increase the blood circulation time, typical for larger 100-200 nm nanoparticles, but also to improve

penetration into deep tumour tissues, which is usually easier for small 4-20 nm particles. In this case, TEM images demonstrate that nanoparticles shrunk from 221 ± 26 nm to 162 ± 22 nm after 24 h and then to 55 ± 4 nm 48 h after laser irradiation at pH = 6.5 (Figure 16B). This shrinkage and decomposition of the nanocapsules into small-sized nano-drugs is thought to be caused by loss of stability inside the nanoparticles, due to changes in interaction between the internal interface of the nanocapsules and water molecules by intermolecular forces of PPP and the degradation of ester and amide bonds in PPP at low pH. While the large nanoparticles remained in blood for longer, the small-nanodrugs could enter tumours and produce ROS by Fe<sup>2+</sup>-catalysed Fenton reaction while delivering DOX and ICG to cancer cells. The accumulation of nanocapsules at the tumour site was evaluated *in vivo* with T<sub>2</sub>-weighted MRI of KB tumour-bearing mice in the presence and absence of a laser (Figure 16C-F). Results show that ICG@Fe/FeO-PPP-FA nanocapsules enhance the T<sub>2</sub> signal intensity and make the tumour region darker than the non-targeted nanocapsules, after 24 h of injection. The contrast enhancement at the tumour site was even

more pronounced after treatment with a laser, which suggested that the laser-triggered shrinkage of the DOX-ICG@Fe/FeO-PPP nanocapsules either induced deep tissue penetration of the theranostic agent or changed the relaxometric properties of the nanoparticles. The *in vivo* efficacy of these agents for cancer therapy revealed that injection of the nanocapsules followed by laser irradiation (808 nm,  $0.3 \text{ W cm}^{-2}$ ) was sufficient to eradicate KB tumours in mice (Figure 16G).

Overall, these results showed that the size-switchable strategy had a positive effect on the combinatorial therapy outcome and could, in the future, be adapted to fit a larger range of other functions while maintaining a multi-triggered controllable smart design.

## Conclusion and Future Perspectives

Cancer theranostics has emerged as a very

promising multi-disciplinary field that is responsible for narrowing the divide between biomedical sciences, medical imaging and nanotechnology. Although theranostics is still a new field, and relatively unexplored, it is already paving the way for the advancement of personalised medicine and thus, is indirectly contributing to the improvement of the clinical care quality.

Smart cancer theranostics go a step further by providing a more controlled and more informative method to deliver drugs specifically to cancer cells by exploring biochemical shifts between healthy and pathological tissues. Additionally, MRI-assisted responsive theranostics make use of the best parts of MRI, such as minimal invasiveness, high tissue penetration, high spatial resolution and ability to better detect soft tissue pathologies, and, when necessary, can be combined with other imaging modalities to overcome the technique's known

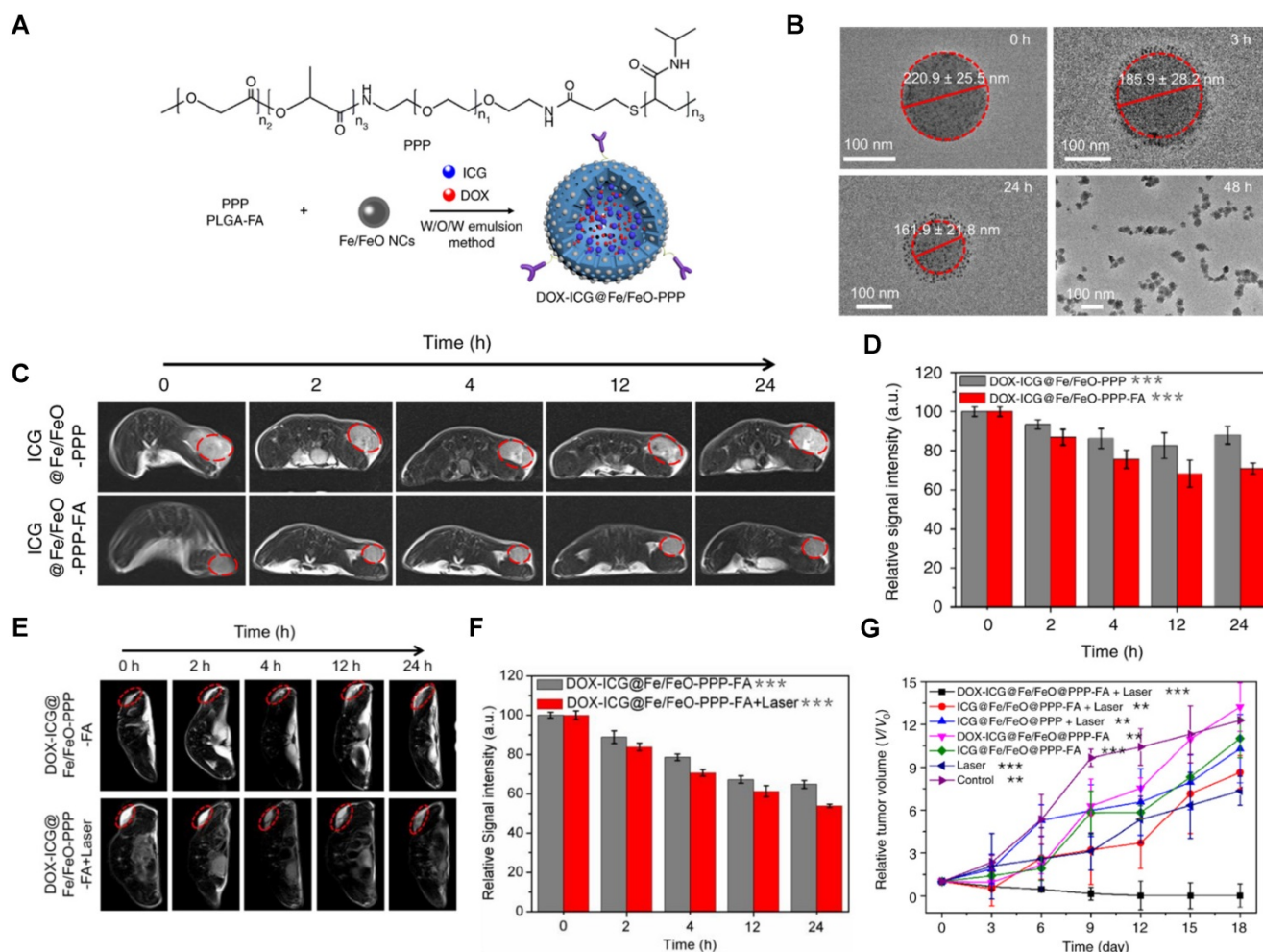


**Figure 16.** A. Fabrication of DOX-ICG@Fe/FeO-PPP nanocapsules. B. TEM image of the shrinking process for DOX-ICG@Fe/FeO-PPP nanocapsules 48 h after the irradiation of laser (808 nm,  $0.3 \text{ W cm}^{-2}$ ) for 5 min (pH = 6.5). C. Real-time MRI of KB tumour-bearing mice after intravenous injection of ICG@Fe/FeO-PPP nanocapsules and ICG@Fe/FeO-PPP-FA nanocapsules at 3 T. D. The relative MRI signal intensities changing at the tumour site after intravenous injection of ICG@Fe/FeO-PPP nanocapsules and ICG@Fe/FeO-PPP-FA nanocapsules, respectively. E. Real-time MRI of KB tumour-bearing mice after intravenous injection of DOX-ICG@Fe/FeO-PPP-FA nanocapsules without and with the irradiation of laser (808 nm,  $0.3 \text{ W cm}^{-2}$ , 5 min) respectively, at 3 T. F. The relative MRI signal intensities changing at the tumour site. G. Volume change of tumour in the different treatments (five mice per group). Adapted with permission from reference [106], copyright 2019 Springer Nature.

sensitivity limitations. The combination with other imaging modalities is made easier by the impressive repertoire of strategies that have been employed in the preparation of responsive and/or dual modal contrast agents for MRI.

In this review, different design strategies employed to prepare smart theranostic agents were presented, including small-molecule and nanoparticle-based approaches (Table 1). The latter are by far the more common strategy in the theranostics field, for several reasons. First, in terms of synthesis, it is easier to equip these nanosystems with multiple functions, whether targeting agents and/or more than one imaging or therapeutic modality, than small-molecule agents. Nanoparticle-based platforms can also be more controllable in terms of blood circulation half-life and target specific accumulation. Still, the mechanism of drug release and MRI signal switch of small molecule theranostics can be more straightforward than their nanosized counterparts. Although several nanoparticle systems have been reported in this review, the most extensively studied and effective in delivering therapeutic efficacy and higher contrast enhancement appear to be polymeric nanoparticles [32, 35, 105, 106, 113, 116, 117, 148, 172]. This is likely related to the possibility of better controlling the drug and/or CA load during the adsorption, entrapment or encapsulation processes. An interesting subset of this smart theranostics repertoire includes externally responsive nanocarriers that transport small molecules into tumour cells, like the work of Wang *et al* [106]. This kind of work can pave way for more controllable, perhaps multi-stimuli responsive systems that can release drugs or even other small-molecule theranostics safely to target sites, before activating those functions *in situ*.

Of the several responsive strategies of smart theranostics that have been presented here, only a few exhibit trigger-switchable MRI contrast enhancement. Theranostics featuring imaging agents that switch “on” or “off” after reaching the target of interest can provide valuable molecular information, that is not attainable with constructs bearing smart therapeutic effectors alone. The most successful theranostics featuring responsive contrast enhancement reported to date have been ESION or Mn<sup>2+</sup>-based nanosystems in which an internal stimuli triggers either an on/ON or OFF/ON switch of the MRI contrast enhancement [105, 113, 148]. The higher efficacy of these turn “on” switches, when compared to turn “off” systems, in which the relaxivity decreases in response to the biological event, is reflected in a boosting of contrast enhancement upon reaching the target tissue, which

can, in the case of theranostics, greatly facilitate drug response evaluation. In theranostics with OFF/ON, the drug release evaluation is especially accurate, since the *in vivo* signal enhancement is likely caused almost entirely in response to the stimulus and not due to a higher accumulation of the contrast agents in the tumours (as could happen in on/ON switches). Although this review shows some successful examples of theranostics with environmentally switchable CAs, future attempts at designing smart theranostic platforms should make use of the wide range of previously reported responsive MRI CAs to prepare smarter theranostic agents. Focusing specifically on the design of theranostics with an OFF/ON switch might also improve the accuracy of the drug release evaluation and thus better estimate the therapeutic outcome. Indeed, innovation in the design of MR theranostics inspired by some of the previously reported remotely activated MR CAs [52, 176] might yield theranostic systems equipped with switchable contrast enhancement induced by external triggers.

Regarding therapy, a large majority of the reported theranostics employ chemotherapy drugs in their designs, which is expected, since chemotherapy is the second most common cancer treatment in the UK, according to Cancer Research UK, following surgery. In these designs, the chemotherapy drug is usually released in response to a tumour microenvironment trigger. However, in some theranostics, the chemotherapy drug is released in response to an external trigger [35, 41]. In this case, chemotherapy is used in combination with either PDT, PTT or MH. The combination of different types of therapies has a synergetic effect in several theranostic systems [35, 41, 106, 118]. As such, future designs should attempt to combine at least two distinct types of activatable cancer therapy that are responsive to environmental and/or external triggers.

Overall, smart theranostic systems tend to be more therapeutically efficient and more diagnostically informative when they combine responsive therapy and switchable imaging simultaneously. Having multiple trigger responsive systems might also be helpful, in particular for therapy, as the combination of chemotherapy with a temperature-increasing therapeutic modality, such as PTT or MH, can make cancer cells more susceptible to drugs and thus improve the treatment outcome. Additionally, smart theranostic systems should strive to include switchable CAs in their design, as they can provide valuable information on cancer progression and treatment response.

**Table 4.** Summary table of the smart theranostics discussed in this review and their imaging and therapeutic modalities, responsive triggers, targeting strategies and MRI properties

Smart theranostic	Classification	Imaging Modality	Therapy	Responsive trigger	Targeting strategy	Type of MRI CAs	$r_1$ or $r_2$ ( $\text{mM}^{-1} \text{s}^{-1}$ )	Ref
PMN/Ce6	Environmentally switchable CAs; Remotely activated therapy.	MRI FL	PDT	pH	EPR effect	$T_1$ (ESIONs)	$r_1 = 3.307$ (pH = 7.4, 1.5 T) $r_1 = 3.87$ (pH = 5.5, 1.5 T)	[113]
DOX@ES-MION3@RGD <sub>2</sub> @mPEG3	Environmentally activated therapy	MRI	Chemo	pH	Ligand targeting	$T_1$ (ESIONs)	$r_1 = 2.34$ (7 T)	[119]
Gd <sub>2</sub> O <sub>3</sub> @MSN-DOX	Environmentally switchable CAs; Environmentally activated therapy.	MRI	Chemo	pH	Ligand targeting	$T_1$ (Gd <sup>3+</sup> )	$r_1 = 9.14$ (3 T)	[115]
MTX-Mn@PEG	Environmentally activated therapy	MRI	Chemo	pH	EPR effect	$T_1$ (Mn <sup>2+</sup> )	$r_1 = 7.76$ (0.5 T)	[117]
SPA-SPIO-IR780	Remotely activated therapy	MRI NIFI	PDT	pH	EPR effect	$T_2$ (SPIONs)	$r_2 = 254.09$ (1.5 T)	[116]
Fe <sub>3</sub> O <sub>4</sub> @TA-PEG/ICG	Environmentally switchable CAs; Remotely activated therapy.	MRI FL	PTT	pH ATP	EPR effect	$T_2$ (SPIONs)	$r_2 = 251.2$ (pH = 7.4, 0.5 T) $r_2 = 13.68$ (pH = 5.5, 10 mM ATP, 0.5 T)	[32]
Bi-MSx-PEG/DOX NFs	Environmentally activated therapy; Remotely activated therapy.	MRI CT PA	PTT; PDT; RT; Chemo (DOX)	pH NIR light X-rays	EPR effect	$T_1$ (Mn <sup>2+</sup> )	$r_1 = 2.60$ (0.5 T)	[118]
MCDION-Se	Environmentally switchable CAs; Environmentally activated therapy.	MRI	CDT	pH	EPR effect	$T_1$ (Mn <sup>2+</sup> )	$r_1 = 2.7$ (pH = 7.4, 9.4 T) $r_1 = 7.1$ (pH = 5.5, 9.4 T)	[128]
Gd-texaphyrin-DOX complex	Environmentally switchable imaging (FL); Environmentally activated therapy.	MRI FL	Chemo	pH	EPR effect	$T_1$ (Gd <sup>3+</sup> )	$r_1 = 20.0$ (1.4 T)	[132]
GdL complexes	Environmentally activated therapy	MRI	Chemo (Cisplatin)	Redox	EPR effect	$T_1$ (Gd <sup>3+</sup> )	$r_1 = 6.3$ (0.5 T)	[137]
Gd-DOTA-Biotin-CPT complex	Environmentally switchable imaging (FL); Environmentally activated therapy.	MRI FL	Chemo (CPT)	Redox	Ligand targeting	$T_1$ (Gd <sup>3+</sup> )	$r_1 = 8.3$ (0.5 T)	[140]
HSPt-PEG-SPION	Environmentally activated therapy	MRI	Chemo (Cisplatin)	Redox	EPR effect	$T_2$ (SPIONs)	$r_2 = 228.96$ (0.5 T)	[147]
DOX/MnO <sub>2</sub> @PVCL NGs	Environmentally switchable CAs; Environmentally activated therapy	MRI	Chemo (DOX)	Redox	EPR effect UTMD	$T_1$ (Mn <sup>2+</sup> )	$r_1 = 0.04$ (no GSH, 0.5 T); $r_1 = 8.33$ (10 mM GSH)	[148]
Magnetic AuNWs	Environmentally switchable CAs; Remotely activated therapy	MRI PA	PTT	Redox NIR light	EPR effect	$T_1$ (ESIONs)	$r_1 = 1.1$ ; $r_2 = 198.6$ (no GSH, 7 T); $r_1 = 3.2$ ; $r_2 = 33.9$ (10 mM GSH)	[105]
NP-RGD	Environmentally switchable imaging (FL); Remotely activated therapy	MRI FL	PDT	Redox NIR light	Ligand targeting	$T_1$ (Gd <sup>3+</sup> )	$r_1 = 20.0$ (0.5 T)	[153]
MS@MnO <sub>2</sub> -CPT NPs	Environmentally switchable CAs; Environmentally activated therapy	MRI	CDT Chemo (CPT)	Redox	EPR effect	$T_1$ (Mn <sup>2+</sup> )	$r_1 = 0.5$ (no GSH); $r_1 = 6.91$ (1 mM GSH)	[154]
PAA-IONPs	Environmentally switchable imaging (FL); Environmentally activated therapy	MRI FL	Chemo (Taxol)	Enzyme (esterase) pH	Ligand targeting	$T_2$ (SPIONs)	$r_2 = 202.0$ (0.5 T)	[160]
ATF-IONP-Gem	Environmentally activated therapy	MRI	Chemo (Gem)	Enzyme (cathepsin B)	Ligand targeting	$T_2$ (SPIONs)	$r_2 = 195$ (3 T)	[157]
pHPMA-Gd-PTX-Cy5.5	Environmentally activated therapy	MRI FL	Chemo (PTX)	Enzyme (cathepsin B)	EPR effect	$T_1$ (Gd <sup>3+</sup> )	$r_1 = 12.9$ (1.5 T)	[158]
BP-PTX Gd NPs	Environmentally activated therapy	MRI FL	Chemo (PTX)	Enzyme (cathepsin B)	EPR effect	$T_1$ (Gd <sup>3+</sup> )	$r_1 = 8.6$ (1.5 T)	[28]
T-MAN	Remotely activated therapy; Environmentally activated imaging (FL)	MRI FL	PTT	Enzyme (MMP-2)	Ligand targeting	$T_1$ (Gd <sup>3+</sup> )	$r_1 = 60.0$ (1 T)	[162]
Mn <sup>2+</sup> -PDA @DOX/PLGA	Remotely activated therapy	MRI	Chemo (DOX) PTT	Temp. NIR light	EPR effect	$T_1$ (Mn <sup>2+</sup> )	$r_1 = 30.49$ (0.5 T)	[35]
mWNVs	Remotely activated therapy	MRI	Chemo (OncoA) MH	Temp. AMF	EPR effect	$T_2$ (SPIONs)	$r_2 = 930$ (1.4 T)	[41]
PFH/DOX@PLGA/Fe <sub>3</sub> O <sub>4</sub> -FA	Remotely activated therapy; Remotely activated imaging (US)	MRI US	Chemo (DOX) HIFU	HIFU	Ligand targeting	$T_2$ (SPIONs)	-	[166]
Gado-Doxo-Lipo	Remotely activated therapy	MRI	Chemo (DOX)	US	EPR	$T_1$ (Gd <sup>3+</sup> )	-	[167, 168]
MFMSN-Ce6	Remotely activated therapy	MRI	PDT	NIR light	EPR effect	$T_1$ (Mn <sup>2+</sup> )	$r_1 = 60.9$ (3 T)	[172]
CuS-MnS <sub>2</sub>	Remotely activated therapy	MRI	PTT PDT	NIR light	EPR effect	$T_1$ (Mn <sup>2+</sup> )	$r_1 = 28.5$ (3 T)	[40]
DOX-ICG@Fe/FeO-PPP-FA	Remotely activated therapy; Environmentally activated	MRI	PDT; Chemo (DOX)	NIR light pH	Ligand targeting	$T_2$ (SPIONs)	$r_2 = 130$ (3 T)	[106]

Smart theranostic	Classification	Imaging Modality	Therapy	Responsive trigger	Targeting strategy	Type of MRI CAs	$r_1$ or $r_2$ ( $\text{mM}^{-1} \text{s}^{-1}$ )	Ref
	therapy							

Regarding the targeting strategies, Table 1 shows that passive targeting through the EPR effect is the most common amongst the provided examples. Targeting tumour tissues *via* EPR has proven successful for a variety of nanomedicines and nanotheranostics [177]. Nonetheless, since the EPR effect depends on the tumours' leaky vasculature resulting from rapid angiogenesis and poorly developed lymphatic drainage system, it is highly conditioned by individual heterogeneity and by the stage of the malignancy [177-180]. The blood circulation time of the theranostic agents can also impact tumour uptake. These factors will undoubtedly influence the accumulation of theranostic agents in target tissues and thus greatly impact the imaging and therapeutic efficiency of the constructs. Smart theranostics with active targeting components, such as ligands, might allow for early malignancy detection. Still, since most biochemical targets exist in the body at very low concentrations (e.g. receptors exist in membranes in concentrations ranging from  $10^{-9}$  to  $10^{-3}$  mol  $\text{g}^{-1}$  of tissue) [181], the imaging and therapeutic efficiency of these theranostics can be hindered unless a strategy is applied to ensure the minimal theranostic concentration threshold for therapeutic and imaging purposes is reached. This can be achieved by increasing the theranostic payload by using ratiometric approaches to conjugate multiple theranostic agents to a single targeting vector in order to increase the local concentration of a theranostic, or by making use of endogenous biological processes, such as passive transport, receptor-mediated internalisation, or endocytosis, to promote the intracellular accumulation of these agents.

While the future is bright and some of these responsive theranostic probes could be very promising in the growing era of personalised medicine, some hardships still need to be surmounted before clinical application. The discrepancy between the dose of contrast agent that needs to be administered to enhance MRI signal and the concentration of biological target or endogenous stimuli is one of the major obstacles. Not only does the solution require intelligent design of theranostics to ensure sufficient local contrast enhancement, but it also demands the agent to be manufactured in bulk and pass rigorous preclinical safety studies. The latter would obviously require a major investment, which might be difficult to obtain for tailored theranostic agents that would probably only be effective in a

subset of patients. There are other barriers preventing the clinical application of responsive MRI theranostics, including concerns about their reproducibility. Environmentally responsive theranostics respond to internal triggers, which might be heterogenous between patients and might greatly vary in concentration, thus possibly hindering the reproducibility of these constructs. Remotely activated theranostics might, in theory, provide more reproducible outcomes, unless the pharmacokinetics and biodistribution of the theranostics varies considerably between individuals. Still, these responsive MR theranostic platforms could help with the treatment of a wide range of pathologies that stretch a lot further beyond cancer. Even though breakthroughs in this field are highly dependent on the cooperation between different areas of knowledge, the future of smart theranostics is promising.

## Acknowledgements

The authors would like to acknowledge the financial support from the Medical Research Council (MR/T002573/1), the University of Hull and the International Iberian Nanotechnology laboratory. We also acknowledge financial support by NORTE 2020 (2014-2020 North Portugal Regional Operational Program) and the ERDF (European Regional Development Fund) under Grant NORTE-01-0145-FEDER-000019, by the "Fundação para a Ciência e a Tecnologia" and the ERDF by NORTE 2020 through the projects UTAP-EXPL/NTec/0038/2017 (NANOTHER - TAMs-targeted and externally controlled nanotheranostics of triple-negative-breast-cancer), NORTE-01-0145-FEDER-031142 (MAGTARGETON - Local specific treatment of triple-negative-breast-cancer through externally triggered target-less drug carriers), NORTE-01-0145-FEDER-028052 (SELF-I - Self-reporting immunostimulating formulation for on-demand cancer therapy with real time treatment response monitoring), and by 2014-2020 INTERREG Cooperation Programme Spain-Portugal (POCTEP) through the project 0624\_2IQBIONEURO\_6\_E.

## Competing Interests

The authors have declared that no competing interest exists.

## References

1. Kelkar SS, Reineke TM. Theranostics: Combining Imaging and Therapy. *Bioconjugate Chemistry*. 2011; 22: 1879-903.

2. Jeong Y, Hwang HS, Na K. Theranostics and contrast agents for magnetic resonance imaging. *Biomaterials research*. 2018; 22: 20.
3. Shanbhag PP, Jog SV, Chogale MM, Gaikwad SS. Theranostics for cancer therapy. *Current drug delivery*. 2013; 10: 357-62.
4. Sharma R, Mody N, Agrawal U, Vyas S. Theranostic nanomedicine; a next generation platform for cancer diagnosis and therapy. *Mini reviews in medicinal chemistry*. 2017; 17: 1746-57.
5. Ramanathan S, Archunan G, Sivakumar M, Selvan ST, Fred AL, Kumar S, et al. Theranostic applications of nanoparticles in neurodegenerative disorders. *International journal of nanomedicine*. 2018; 13: 5561.
6. Li Y, Liu R, Ji W, Li Y, Liu L, Zhang X. Delivery systems for theranostics in neurodegenerative diseases. *Nano Research*. 2018; 11: 5535-55.
7. Sharma M, Dube T, Chibh S, Kour A, Mishra J, Panda JJ. Nanotheranostics, a future remedy of neurological disorders. *Expert opinion on drug delivery*. 2019; 16: 113-28.
8. Tang J, Lobatto ME, Read JC, Mieszawska AJ, Fayad ZA, Mulder WJM. Nanomedical Theranostics in Cardiovascular Disease. *Curr Cardiovasc Imaging Rep*. 2012; 5: 19-25.
9. Cattaneo M, Froio A, Gallino A. Cardiovascular Imaging and Theranostics in Cardiovascular Pharmacotherapy. *Eur Cardiol*. 2019; 14: 62-4.
10. Gong N, Zhang Y, Teng X, Wang Y, Huo S, Qing G, et al. Proton-driven transformable nanovaccine for cancer immunotherapy. *Nature nanotechnology*. 2020; 15: 1053-64.
11. Shen Z, Liu T, Li Y, Lau J, Yang Z, Fan W, et al. Fenton-reaction-acceleratable magnetic nanoparticles for ferroptosis therapy of orthotopic brain tumors. *ACS nano*. 2018; 12: 11355-65.
12. Muthu MS, Leong DT, Mei L, Feng S-S. Nanotheranostics- application and further development of nanomedicine strategies for advanced theranostics. *Theranostics*. 2014; 4: 660.
13. Shi C, Zhou Z, Lin H, Gao J. Imaging Beyond Seeing: Early Prognosis of Cancer Treatment. *Small Methods*. 2020: 2001025.
14. Gao Z, Mu W, Tian Y, Su Y, Sun H, Zhang G, et al. Self-assembly of paramagnetic amphiphilic copolymers for synergistic therapy. *Journal of Materials Chemistry B*. 2020.
15. Li Z, Zhu L, Liu W, Zheng Y, Li X, Ye J, et al. Near-infrared/pH dual-responsive nanoconjugates for targeted imaging and chemo/gene/photothermal tri-therapies of non-small cell lung cancer. *Acta Biomaterialia*. 2020; 107: 242-59.
16. Guo Y, Jiang K, Shen Z, Zheng G, Fan L, Zhao R, et al. A Small Molecule Nanodrug by Self-Assembly of Dual Anticancer Drugs and Photosensitizer for Synergistic near-Infrared Cancer Theranostics. *ACS Applied Materials & Interfaces*. 2017; 9: 43508-19.
17. Fleuren ED, Versleijen-Jonkers YM, Heskamp S, van Herpen CM, Oyen WJ, van der Graaf WT, et al. Theranostic applications of antibodies in oncology. *Molecular oncology*. 2014; 8: 799-812.
18. Dammes N, Peer D. Monoclonal antibody-based molecular imaging strategies and theranostic opportunities. *Theranostics*. 2020; 10: 938.
19. Aghvliyan S, Lu Y, Winnik MA, Hedley DW, Reilly RM. Panitumumab modified with metal-chelating polymers (MCP) complexed to 111In and 177Lu—An EGFR-targeted theranostic for pancreatic cancer. *Molecular pharmaceutics*. 2018; 15: 1150-9.
20. Asati S, Pandey V, Soni V. RGD Peptide as a Targeting Moiety for Theranostic Purpose: An Update Study. *International Journal of Peptide Research and Therapeutics*. 2019; 25: 49-65.
21. Panikar SS, Ramirez-García G, Vallejo-Cardona AA, Banu N, Patrón-Soberano OA, Cialla-May D, et al. Novel anti-HER2 peptide-conjugated theranostic nanoliposomes combining NaYF<sub>4</sub>:Yb,Er nanoparticles for NIR-activated bioimaging and chemo-photodynamic therapy against breast cancer. *Nanoscale*. 2019; 11: 20598-613.
22. Shen Z, Liu T, Yang Z, Zhou Z, Tang W, Fan W, et al. Small-sized gadolinium oxide based nanoparticles for high-efficiency theranostics of orthotopic glioblastoma. *Biomaterials*. 2020; 235: 119783.
23. Khalid U, Vi C, Henri J, Macdonald J, Eu P, Mandarano G, et al. Radiolabelled Aptamers for Theranostic Treatment of Cancer. *Pharmaceutics*. 2019; 12: 2.
24. Kaur H, Bruno JG, Kumar A, Sharma TK. Aptamers in the therapeutics and diagnostics pipelines. *Theranostics*. 2018; 8: 4016.
25. Tran PH, Xiang D, Nguyen TN, Tran TT, Chen Q, Yin W, et al. Aptamer-guided extracellular vesicle theranostics in oncology. *Theranostics*. 2020; 10: 3849.
26. Calderera-Moore ME, Liechty WB, Peppas NA. Responsive Theranostic Systems: Integration of Diagnostic Imaging Agents and Responsive Controlled Release Drug Delivery Carriers. *Accounts of Chemical Research*. 2011; 44: 1061-70.
27. Augustine R, Kalva N, Kim HA, Zhang Y, Kim I. pH-Responsive Polypeptide-Based Smart Nano-Carriers for Theranostic Applications. *Molecules (Basel, Switzerland)*. 2019; 24: 2961.
28. Cai H, Dai X, Wang X, Tan P, Gu L, Luo Q, et al. A Nanostrategy for Efficient Imaging-Guided Antitumor Therapy through a Stimuli-Responsive Branched Polymeric Prodrug. *Advanced Science*. 2020; 7: 1903243.
29. Mu J, Lin J, Huang P, Chen X. Development of endogenous enzyme-responsive nanomaterials for theranostics. *Chemical Society Reviews*. 2018; 47: 5554-73.
30. Cho MH, Shin SH, Park SH, Kadayakkara DK, Kim D, Choi Y. Targeted, Stimuli-Responsive, and Theranostic 19F Magnetic Resonance Imaging Probes. *Bioconjugate Chemistry*. 2019; 30: 2502-18.
31. Hao Y, Wang L, Zhang B, Li D, Meng D, Shi J, et al. Manganese dioxide nanosheets-based redox/pH-responsive drug delivery system for cancer theranostic application. *International journal of nanomedicine*. 2016; 11: 1759-78.
32. Song X-R, Li S-H, Dai J, Song L, Huang G, Lin R, et al. Polyphenol-Inspired Facile Construction of Smart Assemblies for ATP- and pH-Responsive Tumor MR/Optical Imaging and Photothermal Therapy. *Small*. 2017; 13: 1603997.
33. Mi P. Stimuli-responsive nanocarriers for drug delivery, tumor imaging, therapy and theranostics. *Theranostics*. 2020; 10: 4557.
34. Penet M-F, Krishnamachary B, Chen Z, Jin J, Bhujwala ZM. Chapter Seven - Molecular Imaging of the Tumor Microenvironment for Precision Medicine and Theranostics. In: Pomper MG, Fisher PB, editors. *Advances in Cancer Research*: Academic Press; 2014. p. 235-56.
35. Xi J, Da L, Yang C, Chen R, Gao L, Fan L, et al. Mn(2+)-coordinated PDA@DOX/PLGA nanoparticles as a smart theranostic agent for synergistic chemo-photothermal tumor therapy. *International journal of nanomedicine*. 2017; 12: 3331-45.
36. Hou Z, Zhang Y, Deng K, Chen Y, Li X, Deng X, et al. UV-Emitting Upconversion-Based TiO<sub>2</sub> Photosensitizing Nanoplatform: Near-Infrared Light Mediated in Vivo Photodynamic Therapy via Mitochondria-Involved Apoptosis Pathway. *ACS Nano*. 2015; 9: 2584-99.
37. Yang Y, Liu J, Liang C, Feng L, Fu T, Dong Z, et al. Nanoscale Metal-Organic Particles with Rapid Clearance for Magnetic Resonance Imaging-Guided Photothermal Therapy. *ACS Nano*. 2016; 10: 2774-81.
38. Karimi M, Sahandi Zangabad P, Baghaee-Ravari S, Ghazadeh M, Mirshekari H, Hamblin MR. Smart Nanostructures for Cargo Delivery: Uncaging and Activating by Light. *Journal of the American Chemical Society*. 2017; 139: 4584-610.
39. Zhu H, Cao X, Cai X, Tian Y, Wang D, Qi J, et al. Pifithrin- $\mu$  incorporated in gold nanoparticle amplifies pro-apoptotic unfolded protein response cascades to potentiate synergistic glioblastoma therapy. *Biomaterials*. 2020; 232: 119677.
40. Chen W, Wang X, Zhao B, Zhang R, Xie Z, He Y, et al. CuS-MnS 2 nano-flowers for magnetic resonance imaging guided photothermal/photodynamic therapy of ovarian cancer through necroptosis. *Nanoscale*. 2019; 11: 12983-9.
41. de Moura CL, Gallo J, García-Hevia L, Pessoa ODL, Ricardo NMPS, Bañobre-López M. Magnetic Hybrid Wax Nanocomposites as Externally Controlled Theranostic Vehicles: High MRI Enhancement and Synergistic Magnetically Assisted Thermo/Chemo Therapy. *Chemistry - A European Journal*. 2020; 26: 4531-8.
42. Moran CM, Thomson AJW. Preclinical Ultrasound Imaging—A Review of Techniques and Imaging Applications. *Frontiers in Physics*. 2020; 8.
43. Stylogiannis A, Prade L, Buehler A, Aguirre J, Sergiadis G, Ntziachristos V. Continuous wave laser diodes enable fast optoacoustic imaging. *Photoacoustics*. 2018; 9: 31-8.
44. Picillo M, Abate F, Ponticorvo S, Tepedino MF, Errò R, Frosini D, et al. Association of MRI measures with disease severity and progression in Progressive Supranuclear Palsy. *Frontiers in neurology*. 2020; 11.
45. Cheng X, Li H, Chen Y, Luo B, Liu X, Liu W, et al. Ultrasound-triggered phase transition sensitive magnetic fluorescent nanodroplets as a multimodal imaging contrast agent in rat and mouse model. *PLoS One*. 2013; 8: e85003.
46. Tang S, Du Q, Liu T, Tan L, Niu M, Gao L, et al. In vivo magnetic resonance imaging and microwave thermotherapy of cancer using novel chitosan microcapsules. *Nanoscale research letters*. 2016; 11: 1-8.
47. Qiu L, Wang W, Li K, Peng Y, Lv G, Liu Q, et al. Rational design of caspase-responsive smart molecular probe for positron emission tomography imaging of drug-induced apoptosis. *Theranostics*. 2019; 9: 6962-75.
48. Zhao X, Yang C-X, Chen L-G, Yan X-P. Dual-stimuli responsive and reversibly activatable theranostic nanoprobe for precision tumor-targeting and fluorescence-guided photothermal therapy. *Nature Communications*. 2017; 8: 14998.
49. Yang X, Shi X, Ji J, Zhai G. Development of redox-responsive theranostic nanoparticles for near-infrared fluorescence imaging-guided photodynamic/chemotherapy of tumor. *Drug Deliv*. 2018; 25: 780-96.
50. Keum DH, Mun JH, Hwang BW, Kim J, Kim H, Jo W, et al. Smart Microbubble Eluting Theranostic Stent for Noninvasive Ultrasound Imaging and Prevention of Restenosis. *Small*. 2017; 13: 1602925.
51. Parodi A, Rudzinska M, Leporatti S, Anissimov Y, Zamyatnin Jr AA. Smart nanotheranostics responsive to pathological stimuli. *Frontiers in Bioengineering and Biotechnology*. 2020; 8: 503.
52. Wahsner J, Gale EM, Rodriguez-Rodriguez A, Caravan P. Chemistry of MRI Contrast Agents: Current Challenges and New Frontiers. *Chem Rev*. 2018.
53. De León-Rodríguez LM, Martins AF, Pinho MC, Rofsky NM, Sherry AD. Basic MR relaxation mechanisms and contrast agent design. *Journal of Magnetic Resonance Imaging*. 2015; 42: 545-65.
54. Katti G, Ara S, Shireen D. Magnetic resonance imaging (MRI) - A review. *Intl J Dental Clin*. 2011; 3.
55. Grover VP, Tognarelli JM, Crosse MM, Cox IJ, Taylor-Robinson SD, McPhail MJ. Magnetic resonance imaging: principles and techniques: lessons for clinicians. *Journal of clinical and experimental hepatology*. 2015; 5: 246-55.
56. Weishaupt D, D. Köchli V, Marincek B. How Does MRI Work?: An Introduction to the Physics and Function of Magnetic Resonance Imaging; 2006.
57. Henderson RG. Nuclear Magnetic Resonance Imaging: A Review1. *Journal of the Royal Society of Medicine*. 1983; 76: 206-12.

58. Amoroso AJ, Pope SJA. Using lanthanide ions in molecular bioimaging. *Chemical Society Reviews*. 2015; 44: 4723-42.
59. Caravan P. Strategies for increasing the sensitivity of gadolinium based MRI contrast agents. *Chemical Society Reviews*. 2006; 35: 512-23.
60. Tirotta I, Dichiarante V, Pigliacelli C, Cavallo G, Terraneo G, Bombelli FB, et al. 19F magnetic resonance imaging (MRI): from design of materials to clinical applications. *Chemical Reviews*. 2014; 115: 1106-29.
61. Bober Z, Aebischer D, Ozóg L, Tabarkiewicz J, Tutka P, Bartusik-Aebischer D. 19F MRI As a tool for imaging drug delivery to tissue and individual cells. 2017.
62. Brown MA, Semelka RC, Dale BM. MRI: basic principles and applications: John Wiley & Sons; 2015.
63. Ridgway J. Cardiovascular magnetic resonance physics for clinicians: Part I; 2010.
64. Brito BP, Thomas W.; Stasiuk, Graeme J. Design of gadolinium complexes as magnetic resonance imaging contrast agents. *Journal of Organometallic Chemistry*. 2021; 43: 83-110.
65. Lowe MP. MRI Contrast Agents: The Next Generation. *Australian Journal of Chemistry*. 2002; 55: 551-6.
66. Lohrke J, Frenzel T, Endrikat J, Alves FC, Grist TM, Law M, et al. 25 years of contrast-enhanced MRI: developments, current challenges and future perspectives. *Advances in therapy*. 2016; 33: 1-28.
67. Lauffer RB. Paramagnetic metal complexes as water proton relaxation agents for NMR imaging: theory and design. *Chemical Reviews*. 1987; 87: 901-27.
68. Xiao Y-D, Paudel R, Liu J, Cong M, Zhang Z-S, Zhou S-K. MRI contrast agents: Classification and application (Review). *International Journal of Molecular Medicine*. 2016; 38.
69. Pan D, Caruthers SD, Senpan A, Schmieder AH, Wickline SA, Lanza GM. Revisiting an old friend: manganese-based MRI contrast agents. *Wiley Interdisciplinary Reviews: Nanomedicine and Nanobiotechnology*. 2011; 3: 162-73.
70. Pan D, Schmieder AH, Wickline SA, Lanza GM. Manganese-based MRI contrast agents: past, present and future. *Tetrahedron*. 2011; 67: 8431.
71. Caravan P, Ellison JJ, McMurry TJ, Lauffer RB. Gadolinium(III) Chelates as MRI Contrast Agents: Structure, Dynamics, and Applications. *Chemical Reviews*. 1999; 99: 2293-352.
72. Bhardwaj K, Pradhan S, Basel S, Clarke M, Brito B, Thapa S, et al. Tunable NIR-II Emitting Silver Chalcogenide Quantum Dots using Thio/Selenourea Precursors: Preparation of MRI/NIR-II Multimodal Imaging Agent. *Dalton Transactions*. 2020.
73. Perry HL, Yoon I-C, Chabloz NG, Molisso S, Stasiuk GJ, Botnar RM, et al. Metallostar Assemblies Based on Dithiocarbamates for Use as MRI Contrast Agents. *Inorganic Chemistry*. 2020; 59: 10813-23.
74. Chabloz NG, Wenzel MN, Perry HL, Yoon IC, Molisso S, Stasiuk GJ, et al. Polyfunctionalised nanoparticles bearing robust gadolinium surface units for high relaxivity performance in MRI. *Chemistry—A European Journal*. 2019; 25: 10895-906.
75. Chabloz NG, Perry HL, Yoon I-C, Coulson AJ, White AJP, Stasiuk GJ, et al. Combined Magnetic Resonance Imaging and Photodynamic Therapy Using Polyfunctionalised Nanoparticles Bearing Robust Gadolinium Surface Units. *Chemistry - A European Journal*. 2020; 26: 4552-66.
76. Keasberry NA, Bañobre-López M, Wood C, Stasiuk GJ, Gallo J, Long NJ. Tuning the relaxation rates of dual-mode T<sub>1</sub>/T<sub>2</sub> nanoparticle contrast agents: a study into the ideal system. 2015; 7: 16119-28.
77. Stasiuk GJ, Minuzzi F, Sae-Heng M, Rivas C, Juretschke HP, Piemonti L, et al. Dual-Modal Magnetic Resonance/Fluorescent Zinc Probes for Pancreatic  $\beta$ -Cell Mass Imaging. *Chemistry—A European Journal*. 2015; 21: 5023-33.
78. Rivas C, Stasiuk GJ, Sae-Heng M, J. Long N. Towards understanding the design of dual-modal MR/fluorescent probes to sense zinc ions. *Dalton Transactions*. 2015; 44: 4976-85.
79. Sung S, Holmes H, Wainwright L, Toscani A, Stasiuk GJ, White AJP, et al. Multimetallic Complexes and Functionalized Gold Nanoparticles Based on a Combination of d- and f-Elements. *Inorganic Chemistry*. 2014; 53: 1989-2005.
80. Rivas C, Stasiuk GJ, Gallo J, Minuzzi F, Rutter GA, Long NJ. Lanthanide(III) Complexes of Rhodamine-DO3A Conjugates as Agents for Dual-Modal Imaging. *Inorganic Chemistry*. 2013; 52: 14284-93.
81. Stasiuk GJ, Tamang S, Imbert D, Gateau C, Reiss P, Fries P, et al. Optimizing the relaxivity of GdIII complexes appended to InP/ZnS quantum dots by linker tuning. *Dalton Trans*. 2013; 42: 8197-200.
82. Stasiuk GJ, Long NJ. The ubiquitous DOTA and its derivatives: the impact of 1, 4, 7, 10-tetraazacyclododecane-1, 4, 7, 10-tetraacetic acid on biomedical imaging. *Chemical Communications*. 2013; 49: 2732-46.
83. Stasiuk GJ, Smith H, Wylezinska-Arridge M, Tremoleda JL, Trigg W, Luthra SK, et al. Gd<sup>3+</sup> cFLFLFK conjugate for MRI: a targeted contrast agent for FPR1 in inflammation. *Chemical Communications*. 2013; 49: 564-6.
84. Stasiuk GJ, Tamang S, Imbert D, Poillot C, Giardiello M, Tisseyre C, et al. Cell-Permeable Ln(III) Chelate-Functionalized InP Quantum Dots As Multimodal Imaging Agents. *ACS Nano*. 2011; 5: 8193-201.
85. Kim BH, Lee N, Kim H, An K, Park YI, Choi Y, et al. Large-scale synthesis of uniform and extremely small-sized iron oxide nanoparticles for high-resolution T<sub>1</sub> magnetic resonance imaging contrast agents. *Journal of the American Chemical Society*. 2011; 133: 12624-31.
86. García-Hevia L, Bañobre-López M, Gallo J. Recent Progress on Manganese-Based Nanostructures as Responsive MRI Contrast Agents. *Chemistry—A European Journal*. 2019; 25: 431-41.
87. Bañobre-López M, García-Hevia L, Cerqueira MF, Rivadulla F, Gallo J. Tunable performance of manganese oxide nanostructures as MRI contrast agents. *Chemistry—A European Journal*. 2018; 24: 1295-303.
88. Shen Z, Song J, Zhou Z, Yung BC, Aronova MA, Li Y, et al. Dotted core-shell nanoparticles for T<sub>1</sub>-weighted MRI of tumors. *Advanced Materials*. 2018; 30: 1803163.
89. Shen Z, Fan W, Yang Z, Liu Y, Bregadze VI, Mandal SK, et al. Exceedingly small gadolinium oxide nanoparticles with remarkable relaxivities for magnetic resonance imaging of tumors. *Small*. 2019; 15: 1903422.
90. Wei Z, Jiang Z, Pan C, Xia J, Xu K, Xue T, et al. Ten-Gram-Scale Facile Synthesis of Organogadolinium Complex Nanoparticles for Tumor Diagnosis. *Small*. 2020; 16: 1906870.
91. Girija AR. 12 - Medical Applications of Polymer/Functionalized Nanoparticle Systems. In: Pielichowski K, Majka TM, editors. *Polymer Composites with Functionalized Nanoparticles*: Elsevier; 2019. p. 381-404.
92. Jin R, Lin B, Li D, Ai H. Superparamagnetic iron oxide nanoparticles for MR imaging and therapy: design considerations and clinical applications. *Current Opinion in Pharmacology*. 2014; 18: 18-27.
93. Zhou Z, Yang L, Gao J, Chen X. Structure-relaxivity relationships of magnetic nanoparticles for magnetic resonance imaging. *Advanced Materials*. 2019; 31: 1804567.
94. Hingorani DV, Bernstein AS, Pagel MD. A review of responsive MRI contrast agents: 2005-2014. *Contrast media & molecular imaging*. 2015; 10: 245-65.
95. Pinto SM, Tomé V, Calvete MJ, Castro MMC, Tóth É, Galdes CF. Metal-based redox-responsive MRI contrast agents. *Coordination Chemistry Reviews*. 2019; 390: 1-31.
96. Pierre VC, Harris SM, Pailloux SL. Comparing Strategies in the Design of Responsive Contrast Agents for Magnetic Resonance Imaging: A Case Study with Copper and Zinc. *Accounts of Chemical Research*. 2018; 51: 342-51.
97. Eling CJ, Price TW, Marshall AR, Narda Viscomi F, Robinson P, Firth G, et al. A Dual-Modal SERS/Fluorescence Gold Nanoparticle Probe for Mitochondrial Imaging. *ChemPlusChem*. 2017; 82: 674-80.
98. Yue X, Wang Z, Zhu L, Wang Y, Qian C, Ma Y, et al. Novel 19F Activatable Probe for the Detection of Matrix Metalloproteinase-2 Activity by MRI/MRS. *Molecular Pharmaceutics*. 2014; 11: 4208-17.
99. Zhou Z, Deng H, Yang W, Wang Z, Lin L, Munasinghe J, et al. Early stratification of radiotherapy response by activatable inflammation magnetic resonance imaging. *Nat Commun*. 2020; 11: 3032.
100. Liu D, Zhou Z, Wang X, Deng H, Sun L, Lin H, et al. Yolk-shell nanovesicles endow glutathione-responsive concurrent drug release and T<sub>1</sub> MRI activation for cancer theranostics. *Biomaterials*. 2020; 244: 119979.
101. Lin LS, Wang JF, Song J, Liu Y, Zhu G, Dai Y, et al. Cooperation of endogenous and exogenous reactive oxygen species induced by zinc peroxide nanoparticles to enhance oxidative stress-based cancer therapy. *Theranostics*. 2019; 9: 7200-9.
102. Wei R, Gong X, Lin H, Zhang K, Li A, Liu K, et al. Versatile Octapod-Shaped Hollow Porous Manganese(II) Oxide Nanoplatforam for Real-Time Visualization of Cargo Delivery. *Nano Lett*. 2019; 19: 5394-402.
103. Wang S, Zhou Z, Wang Z, Liu Y, Jacobson O, Shen Z, et al. Gadolinium Metallofullerene-Based Activatable Contrast Agent for Tumor Signal Amplification and Monitoring of Drug Release. *Small*. 2019; 15: e1900691.
104. Wang S, Zhou Z, Yu G, Lu N, Liu Y, Dai Y, et al. Gadolinium Metallofullerene-Polypyrrole Nanoparticles for Activatable Dual-Modal Imaging-Guided Photothermal Therapy. *ACS Appl Mater Interfaces*. 2018; 10: 28382-9.
105. Liu Y, Yang Z, Huang X, Yu G, Wang S, Zhou Z, et al. Glutathione-Responsive Self-Assembled Magnetic Gold Nanowreath for Enhanced Tumor Imaging and Imaging-Guided Photothermal Therapy. *ACS Nano*. 2018; 12: 8129-37.
106. Wang Z, Ju Y, Ali Z, Yin H, Sheng F, Lin J, et al. Near-infrared light and tumor microenvironment dual responsive size-switchable nanocapsules for multimodal tumor theranostics. *Nature communications*. 2019; 10: 1-12.
107. Engin K, Leeper D, Cater J, Thistlethwaite A, Tupchong L, McFarlane J. Extracellular pH distribution in human tumours. *International Journal of Hyperthermia*. 1995; 11: 211-6.
108. Hao G, Xu ZP, Li L. Manipulating extracellular tumour pH: an effective target for cancer therapy. *RSC advances*. 2018; 8: 22182-92.
109. Benyettou F, Das G, Nair AR, Prakasam T, Shinde DB, Sharma SK, et al. Covalent Organic Framework Embedded with Magnetic Nanoparticles for MRI and Chemo-Therotherapy. *Journal of the American Chemical Society*. 2020; 142: 18782-94.
110. Chen Y, Ai K, Liu J, Sun G, Yin Q, Lu L. Multifunctional envelope-type mesoporous silica nanoparticles for pH-responsive drug delivery and magnetic resonance imaging. *Biomaterials*. 2015; 60: 111-20.
111. Ye D-X, Ma Y-Y, Zhao W, Cao H-M, Kong J-L, Xiong H-M, et al. ZnO-based nanostructures for labeling and treatment of mouse tumors without detectable toxic side effects. *ACS nano*. 2016; 10: 4294-300.
112. Zhao Z, Wang X, Zhang Z, Zhang H, Liu H, Zhu X, et al. Real-time monitoring of arsenic trioxide release and delivery by activatable T<sub>1</sub> imaging. *ACS nano*. 2015; 9: 2749-59.
113. Ling D, Park W, Park S-j, Lu Y, Kim KS, Hackett MJ, et al. Multifunctional Tumor pH-Sensitive Self-Assembled Nanoparticles for Bimodal Imaging and Treatment of Resistant Heterogeneous Tumors. *Journal of the American Chemical Society*. 2014; 136: 5647-55.

114. Nasongkla N, Bey E, Ren J, Ai H, Khemtong C, Guthi JS, et al. Multifunctional polymeric micelles as cancer-targeted, MRI-ultrasensitive drug delivery systems. *Nano letters*. 2006; 6: 2427-30.
115. He K, Li J, Shen Y, Yu Y. pH-Responsive polyelectrolyte coated gadolinium oxide-doped mesoporous silica nanoparticles (Gd 2 O 3 @ MSNs) for synergistic drug delivery and magnetic resonance imaging enhancement. *Journal of Materials Chemistry B*. 2019; 7: 6840-54.
116. Wang S, Mao J, Liu H, Huang S, Cai J, Gui W, et al. pH-Sensitive nanotheranostics for dual-modality imaging guided nanoenzyme catalysis therapy and phototherapy. *Journal of Materials Chemistry B*. 2020.
117. Wu Y, Xu L, Qian J, Shi L, Su Y, Wang Y, et al. Methotrexate-Mn2+ based nanoscale coordination polymers as a theranostic nanoplatform for MRI guided chemotherapy. *Biomaterials Science*. 2020; 8: 712-9.
118. Ren L, Liu X, Ji T, Deng G, Liu F, Yuan H, et al. "All-in-One" Theranostic Agent with Seven Functions Based on Bi-Doped Metal Chalcogenide Nanoflowers. *ACS Applied Materials & Interfaces*. 2019; 11: 45467-78.
119. Shen Z, Chen T, Ma X, Ren W, Zhou Z, Zhu G, et al. Multifunctional theranostic nanoparticles based on exceedingly small magnetic iron oxide nanoparticles for T 1-weighted magnetic resonance imaging and chemotherapy. *ACS nano*. 2017; 11: 10992-1004.
120. Malhotra N, Lee J-S, Liman RAD, Ruallo JMS, Villaflores OB, Ger T-R, et al. Potential toxicity of iron oxide magnetic nanoparticles: A review. *Molecules*. 2020; 25: 3159.
121. Le Fur M, Caravan P. The biological fate of gadolinium-based MRI contrast agents: a call to action for bioinorganic chemists. *Metallomics*. 2019; 11: 240-54.
122. Rogosnitzky M, Branch S. Gadolinium-based contrast agent toxicity: a review of known and proposed mechanisms. *Biomaterials*. 2016; 29: 365-76.
123. Sun C, Lin H, Gong X, Yang Z, Mo Y, Chen X, et al. DOTA-Branched Organic Frameworks as Giant and Potent Metal Chelators. *Journal of the American Chemical Society*. 2019; 142: 198-206.
124. Botár R, Molnár E, Trencsényi G, Kiss J, Kálmán FK, Tircsó G. Stable and Inert Mn(II)-Based and pH-Responsive Contrast Agents. *Journal of the American Chemical Society*. 2020; 142: 1662-6.
125. Ndiaye D, Sy M, Pallier A, Mème S, de Silva I, Lacerda S, et al. Inside Back Cover: Unprecedented Kinetic Inertness for a Mn2+-Bispidine Chelate: A Novel Structural Entry for Mn2+-Based Imaging Agents (*Angew. Chem. Int. Ed.* 29/2020). *Angewandte Chemie International Edition*. 2020; 59: 12223-.
126. Clough TJ, Jiang L, Wong K-L, Long NJ. Ligand design strategies to increase stability of gadolinium-based magnetic resonance imaging contrast agents. *Nature communications*. 2019; 10: 1-14.
127. High WA, Ayers RA, Cowper SE. Gadolinium is quantifiable within the tissue of patients with nephrogenic systemic fibrosis. *Journal of the American Academy of Dermatology*. 2007; 56: 710-2.
128. Xiao J, Zhang G, Xu R, Chen H, Wang H, Tian G, et al. A pH-responsive platform combining chemodynamic therapy with limotherapy for simultaneous bioimaging and synergistic cancer therapy. *Biomaterials*. 2019; 216: 119254.
129. Kim H-K, Kang M-K, Jung K-H, Kang S-H, Kim Y-H, Jung J-C, et al. Gadolinium complex of DO3A-benzothiazole aniline (BTA) conjugate as a theranostic agent. *Journal of medicinal chemistry*. 2013; 56: 8104-11.
130. Efthimiadou EK, Katsarou ME, Fardis M, Zikos C, Pitsinos EN, Kazantzis A, et al. Synthesis and characterization of novel natural product-Gd (III) MRI contrast agent conjugates. *Bioorganic & medicinal chemistry letters*. 2008; 18: 6058-61.
131. Kalber TL, Kamaly N, Higham SA, Pugh JA, Bunch J, McLeod CW, et al. Synthesis and characterization of a theranostic vascular disrupting agent for in vivo MRI imaging. *Bioconjugate chemistry*. 2011; 22: 879-86.
132. Lee MH, Kim E-J, Lee H, Park SY, Hong KS, Kim JS, et al. Acid-triggered release of doxorubicin from a hydrazone-linked Gd 3+-texasphyrin conjugate. *Chemical Communications*. 2016; 52: 10551-4.
133. Han L, Zhang X-Y, Wang Y-L, Li X, Yang X-H, Huang M, et al. Redox-responsive theranostic nanoplatforms based on inorganic nanomaterials. *Journal of Controlled Release*. 2017; 259: 40-52.
134. Aquilano K, Baldelli S, Ciriolo MR. Glutathione: new roles in redox signaling for an old antioxidant. *Frontiers in pharmacology*. 2014; 5: 196.
135. Jones DP, Carlson JL, Mody Jr VC, Cai J, Lynn MJ, Sternberg Jr P. Redox state of glutathione in human plasma. *Free Radical Biology and Medicine*. 2000; 28: 625-35.
136. Lee MH, Kim E-J, Lee H, Kim HM, Chang MJ, Park SY, et al. Liposomal Texasphyrin Theranostics for Metastatic Liver Cancer. *Journal of the American Chemical Society*. 2016; 138: 16380-7.
137. Zhu Z, Wang X, Li T, Aime S, Sadler PJ, Guo Z. Platinum (II)-Gadolinium (III) Complexes as Potential Single-Molecular Theranostic Agents for Cancer Treatment. *Angewandte Chemie International Edition*. 2014; 53: 13225-8.
138. Thiabaud G, He G, Sen S, Shelton KA, Baze WB, Segura L, et al. Oxaliplatin Pt (IV) prodrugs conjugated to gadolinium-texasphyrin as potential antitumor agents. *Proceedings of the National Academy of Sciences*. 2020; 117: 7021-9.
139. Adams CJ, Meade TJ. Gd (iii)-Pt (iv) theranostic contrast agents for tandem MR imaging and chemotherapy. *Chemical Science*. 2020; 11: 2524-30.
140. Yang Z, Lin H, Huang J, Li A, Sun C, Richmond J, et al. A gadolinium-complex-based theranostic prodrug for in vivo tumour-targeted magnetic resonance imaging and therapy. *Chemical Communications*. 2019.
141. Jahangirian H, Kalantari K, Izadiyan Z, Rafiee-Moghaddam R, Shameli K, Webster TJ. A review of small molecules and drug delivery applications using gold and iron nanoparticles. *International Journal of Nanomedicine*. 2019; 14: 1633.
142. Chen L, Zhou X, Nie W, Zhang Q, Wang W, Zhang Y, et al. Multifunctional Redox-Responsive Mesoporous Silica Nanoparticles for Efficient Targeting Drug Delivery and Magnetic Resonance Imaging. *ACS Applied Materials & Interfaces*. 2016; 8: 33829-41.
143. Chen Y-C, Huang X-C, Luo Y-L, Chang Y-C, Hsieh Y-Z, Hsu H-Y. Non-metallic nanomaterials in cancer theranostics: a review of silica- and carbon-based drug delivery systems. *Science and technology of advanced materials*. 2013; 14: 044407.
144. Chen Y, Xu P, Shu Z, Wu M, Wang L, Zhang S, et al. Multifunctional graphene oxide-based triple stimuli-responsive nanotheranostics. *Advanced Functional Materials*. 2014; 24: 4386-96.
145. Wu Y-F, Wu H-C, Kuan C-H, Lin C-J, Wang L-W, Chang C-W, et al. Multi-functionalized carbon dots as theranostic nanoagent for gene delivery in lung cancer therapy. *Scientific reports*. 2016; 6: 21170.
146. Xiong D, Zhang X, Peng S, Gu H, Zhang L. Smart pH-sensitive micelles based on redox degradable polymers as DOX/GNPs carriers for controlled drug release and CT imaging. *Colloids and Surfaces B: Biointerfaces*. 2018; 163: 29-40.
147. Zhu Z, Wang Z, Hao Y, Zhu C, Jiao Y, Chen H, et al. Glutathione boosting the cytotoxicity of a magnetic platinum (IV) nano-prodrug in tumor cells. *Chemical science*. 2016; 7: 2864-9.
148. Xu F, Zhu J, Lin L, Zhang C, Sun W, Fan Y, et al. Multifunctional PVCL nanogels with redox-responsiveness enable enhanced MR imaging and ultrasound-promoted tumor chemotherapy. *Theranostics*. 2020; 10: 4349-58.
149. Ding Z, Liu P, Hu D, Sheng Z, Yi H, Gao G, et al. Redox-responsive dextran based theranostic nanoparticles for near-infrared/magnetic resonance imaging and magnetically targeted photodynamic therapy. *Biomaterials science*. 2017; 5: 762-71.
150. Zhao J, Yang Y, Han X, Liang C, Liu J, Song X, et al. Redox-sensitive nanoscale coordination polymers for drug delivery and cancer theranostics. *ACS applied materials & interfaces*. 2017; 9: 23555-63.
151. Zhang S, Guo N, Wan G, Zhang T, Li C, Wang Y, et al. pH and redox dual-responsive nanoparticles based on disulfide-containing poly ( $\beta$ -amino ester) for combining chemotherapy and COX-2 inhibitor to overcome drug resistance in breast cancer. *Journal of nanobiotechnology*. 2019; 17: 1-17.
152. Chen H, Li F, Yao Y, Wang Z, Zhang Z, Tan N. Redox Dual-Responsive and O2-Evolving Theranostic Nanosystem for Highly Selective Chemotherapy against Hypoxic Tumors. *Theranostics*. 2019; 9: 90.
153. An R, Cheng X, Wei S, Hu Y, Sun Y, Huang Z, et al. Smart Magnetic and Fluorogenic Photosensitizer Nanoassemblies Enable Redox-Driven Disassembly for Photodynamic Therapy. *Angewandte Chemie*. 2020; 132: 20817-25.
154. Lin LS, Song J, Song L, Ke K, Liu Y, Zhou Z, et al. Simultaneous Fenton-like Ion Delivery and Glutathione Depletion by MnO2-Based Nanoagent to Enhance Chemodynamic Therapy. *Angewandte Chemie International Edition*. 2018; 57: 4902-6.
155. Baig MH, Adil M, Khan R, Dhadi S, Ahmad K, Rabbani G, et al. Enzyme targeting strategies for prevention and treatment of cancer: Implications for cancer therapy. *Seminars in cancer biology*: Elsevier; 2019. p. 1-11.
156. Qi A, Deng L, Liu X, Wang S, Zhang X, Wang B, et al. Gelatin-encapsulated magnetic nanoparticles for pH, redox, and enzyme multiple stimuli-responsive drug delivery and magnetic resonance imaging. *Journal of biomedical nanotechnology*. 2017; 13: 1386-97.
157. Lee GY, Qian WP, Wang L, Wang YA, Staley CA, Satpathy M, et al. Theranostic Nanoparticles with Controlled Release of Gemcitabine for Targeted Therapy and MRI of Pancreatic Cancer. *ACS Nano*. 2013; 7: 2078-89.
158. Cai H, Wang X, Zhang H, Sun L, Pan D, Gong Q, et al. Enzyme-sensitive biodegradable and multifunctional polymeric conjugate as theranostic nanomedicine. *Applied Materials Today*. 2018; 11: 207-18.
159. Wang B, Lv P, Cai H, Li Y, Zhu H, Lui S, et al. Enzyme-Responsive Copolymer as a Theranostic Prodrug for Tumor In Vivo Imaging and Efficient Chemotherapy. *Journal of biomedical nanotechnology*. 2019; 15: 1897-908.
160. Santra S, Kaitanis C, Grimm J, Perez JM. Drug/dye-loaded, multifunctional iron oxide nanoparticles for combined targeted cancer therapy and dual optical/magnetic resonance imaging. *small*. 2009; 5: 1862-8.
161. Rohrer M, Bauer H, Mintonovitch J, Requardt M, Weinmann H-J. Comparison of magnetic properties of MRI contrast media solutions at different magnetic field strengths. *Investigative radiology*. 2005; 40: 715-24.
162. Shi H, Sun Y, Yan R, Liu S, Zhu L, Liu S, et al. Magnetic Semiconductor Gd-Doping CuS Nanoparticles as Activatable Nanoprobes for Bimodal Imaging and Targeted Photothermal Therapy of Gastric Tumors. *Nano Letters*. 2019; 19: 937-47.
163. Hiruta Y, Nemoto R, Kanazawa H. Design and synthesis of temperature-responsive polymer/silica hybrid nanoparticles and application to thermally controlled cellular uptake. *Colloids and Surfaces B: Biointerfaces*. 2017; 153: 2-9.
164. Qiao Z-Y, Zhang R, Du F-S, Liang D-H, Li Z-C. Multi-responsive nanogels containing motifs of ortho ester, oligo (ethylene glycol) and disulfide linkage as carriers of hydrophobic anti-cancer drugs. *Journal of controlled release*. 2011; 152: 57-66.
165. Izadifar Z, Izadifar Z, Chapman D, Babyn P. An Introduction to High Intensity Focused Ultrasound: Systematic Review on Principles, Devices, and Clinical Applications. *Journal of Clinical Medicine*. 2020; 9: 460.

166. Tang H, Guo Y, Peng L, Fang H, Wang Z, Zheng Y, et al. In vivo targeted, responsive, and synergistic cancer nanotheranostics by magnetic resonance imaging-guided synergistic high-intensity focused ultrasound ablation and chemotherapy. *ACS applied materials & interfaces*. 2018; 10: 15428-41.
167. Rizzitelli S, Giustetto P, Cutrin JC, Castelli DD, Boffa C, Ruzza M, et al. Sonosensitive theranostic liposomes for preclinical in vivo MRI-guided visualization of doxorubicin release stimulated by pulsed low intensity non-focused ultrasound. *Journal of Controlled Release*. 2015; 202: 21-30.
168. Rizzitelli S, Giustetto P, Faletto D, Castelli DD, Aime S, Terreno E. The release of Doxorubicin from liposomes monitored by MRI and triggered by a combination of US stimuli led to a complete tumor regression in a breast cancer mouse model. *Journal of Controlled Release*. 2016; 230: 57-63.
169. Chen H, Zhao Y. Applications of light-responsive systems for cancer theranostics. *ACS applied materials & interfaces*. 2018; 10: 21021-34.
170. Cheng L, Wang C, Feng L, Yang K, Liu Z. Functional nanomaterials for phototherapies of cancer. *Chemical reviews*. 2014; 114: 10869-939.
171. Liu L-H, Qiu W-X, Li B, Zhang C, Sun L-F, Wan S-S, et al. A Red Light Activatable Multifunctional Prodrug for Image-Guided Photodynamic Therapy and Cascaded Chemotherapy. *Advanced Functional Materials*. 2016; 26: 6257-69.
172. Kim J, Cho HR, Jeon H, Kim D, Song C, Lee N, et al. Continuous O<sub>2</sub>-Evolving MnFe<sub>2</sub>O<sub>4</sub> Nanoparticle-Anchored Mesoporous Silica Nanoparticles for Efficient Photodynamic Therapy in Hypoxic Cancer. *Journal of the American Chemical Society*. 2017; 139: 10992-5.
173. Chen Q, Yang D, Yu L, Jing X, Chen Y. Catalytic chemistry of iron-free Fenton nanocatalysts for versatile radical nanotherapeutics. *Materials Horizons*. 2020; 7: 317-37.
174. Blanco E, Shen H, Ferrari M. Principles of nanoparticle design for overcoming biological barriers to drug delivery. *Nature biotechnology*. 2015; 33: 941.
175. Dai Y, Xu C, Sun X, Chen X. Nanoparticle design strategies for enhanced anticancer therapy by exploiting the tumour microenvironment. *Chemical Society Reviews*. 2017; 46: 3830-52.
176. Davies G-L, Kramerberger I, Davis JJ. Environmentally responsive MRI contrast agents. *Chemical Communications*. 2013; 49: 9704-21.
177. Golombek SK, May J-N, Theek B, Appold L, Drude N, Kiessling F, et al. Tumor targeting via EPR: Strategies to enhance patient responses. *Advanced drug delivery reviews*. 2018; 130: 17-38.
178. Maeda H, Wu J, Sawa T, Matsumura Y, Hori K. Tumor vascular permeability and the EPR effect in macromolecular therapeutics: a review. *Journal of Controlled Release*. 2000; 65: 271-84.
179. Acharya S, Sahoo SK. PLGA nanoparticles containing various anticancer agents and tumour delivery by EPR effect. *Advanced Drug Delivery Reviews*. 2011; 63: 170-83.
180. Bogdanov A, Jr., Mazzanti ML. Molecular magnetic resonance contrast agents for the detection of cancer: past and present. *Semin Oncol*. 2011; 38: 42-54.
181. Geraldes CFGC, Laurent S. Classification and basic properties of contrast agents for magnetic resonance imaging. *Contrast Media & Molecular Imaging*. 2009; 4: 1-23.